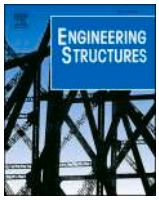
Engineering Structures 327 (2025) 119584



Contents lists available at ScienceDirect

Engineering Structures

journal homepage: www.elsevier.com/locate/engstruct





Experimental and numerical investigation on concrete–filled prefabricated SHCC tubes (CFPSHT) under eccentric compression

Tarek F. El-Shafiey, Mohamed H. Mahmoud, Ahmed T. Baraghith, Mohamed Hindawi *

Structural Engineering Dept., Faculty of Engineering, Tanta University, Tanta, Egypt

ARTICLE INFO

Keywords:
Strain–Hardening Cementitious Composite (SHCC)
Tubular columns
Eccentric loading
Interaction diagrams
Finite element modeling

ABSTRACT

Concrete–filled tubular columns have gained great popularity in the construction of high–rise buildings and bridges. A new type is presented by utilizing a prefabricated reinforced strain–hardening cementitious composite (PSHCC) tube filled with conventional concrete called CFPSHT column. To examine the behavior of the columns under eccentric loading, different eccentricity ratios of 0, 0.125, 0.25, and infinite were considered. The experimental results indicated that the CFPSHT columns resulted in better performance compared to the conventional concrete columns concerning the mode of failure, the load– carrying capacity, and ductility owing to the confinement effect and the high strength of the PSHCC tube. Compared to the conventional concrete columns, the ultimate loads increased by 88 % under concentric loading. Under eccentric loading, the ultimate loads increased in the range of 101–95 %. In addition to experimental work, an analytical load moment interaction of the CFPSHT column was performed and verified with experimental results. Furthermore, the CFPSHT column was simulated through a finite element model (FEM) to further evaluate a wide range of parameters that could affect the behavior of CFPSHT columns and the modeling was refined to take into account the effect of eccentricity on the confinement of the PSHCC tube. The comparisons against the experimental results proved that the proposed FEM simulation could capture the behavior of the CFPSHT columns. Hence, the effects of the SHCC tube thickness and the core concrete strength on the load-moment (P–M) interaction of the CFPSHT column were analyzed.

1. Introduction

Conventional concrete columns are the fundamental component of concrete structures, which are used to support beams and slabs and transmit their loads to the foundation. However, these columns suffer from brittle failure owing to the poor tensile strength, crack resistance, and limited deformability of conventional concrete. Furthermore, with the formation of cracks in concrete columns, steel reinforcement corrosion is likely to occur, especially in corrosive environmental conditions, reducing the durability of these columns. Thus, it is necessary to develop new systems to improve the behavior of such columns.

The constant need to improve the behavior of conventional concrete columns and reduce their sizes in structural systems of buildings led to the widespread of concrete–filled tubular (CFT) columns. Some CFTs were introduced, such as concrete-filled steel tubes (CFSTs) and concrete-filled FRP tubes (CFFTs) [1–5]. The confining effect of steel tube and FRP tube can improve the strength and ductility of these columns [6]. However, some drawbacks exist in CFST and CFFT. In CFST columns, the outer steel tube is vulnerable to corrosion, reducing the compressive and flexural strength [2,7]. In addition, It was found that the post-fire load-carrying capacity of CFST columns could be reduced by up to 50 % compared to those at ambient room temperature without fire exposure [8]. On the other hand, the FRP tube in CFFT columns does not corrode and improve durability, but FRP cannot withstand high temperatures, in addition to poor fire safety and the potential release of toxic gases [9]. Besides, new techniques of CFT columns have been introduced in literature by utilizing cementitious materials as a substitution for outer concrete [10–12].

In the same vein, strain–hardening cementitious composite (SHCC) can be utilized with concrete to produce CFT columns due to its superior properties. SHCC, sometimes called engineered cementitious composite (ECC), was produced first by Li [13] in the early 1990s. The ingredients of SHCC are typically: cement, fine sand, admixtures, and short fibers with a volume fraction percentage of about 2 %. Under uniaxial tension, SHCC shows a strain–hardening behavior with uniformly distributed multiple cracks. SHCC exhibits high tensile strength and strain up to

* Corresponding author.
E-mail address: mohamed_hindawi@f-eng.tanta.edu.eg (M. Hindawi).

https://doi.org/10.1016/j.engstruct.2024.119584
Received 14 August 2024; Received in revised form 19 November 2024; Accepted 26 December 2024
Available online 3 January 2025
0141-0296/Published by Elsevier Ltd.

7.0 MPa and 4 %, respectively [14]. It has a unique deformation performance, unlike concrete, owing to the bridging effect of distributed short fibers. Having reached the tensile strength of the matrix, a multiple cracking behavior and considerable deformation occur, compared to the rapid cracking of concrete once its tensile strength is reached. Hence, SHCC is less permeable than normal concrete; even when cracked, it exhibits tighter crack widths, which may protect reinforcing steel from corrosion and provide more durability [15–20]. Based on the aforementioned properties, SHCC has been applied in many structural applications such as slabs, beams, and columns [21–29].

One of the most economical applications is substituting part of the concrete with SHCC to form a composite combination. Maalej and Li [30] determined that replacing the concrete surrounding the longitudinal reinforcing steel bars, with the ECC in the RC flexural members improved the member durability. Qiao et al. [25] investigated the flexural behavior of U−shaped ECC permanent formwork composite beams with different interfacial preparations. They discovered that using a U−shaped precast ECC layer increased ductility, but had a less significant effect on flexural capacities. Some conducted cyclic experiments on columns using ECC jackets [31–35] and revealed that the ductility and energy dissipation capacity could be increased significantly even with a reduced amount of ECC. According to Pan et al. [26], ECC could be used as permanent formwork for RC columns without applying any surface treatments to the smooth ECC formwork and the core concrete. The results proved that the composite column had better ductility and energy dissipation than the conventional RC column under cyclic loading. However, the appropriate thickness of the ECC tube and the strength of the concrete core were not introduced. Cai et al. [36] examined the behavior of ECC−encased CFST composite columns under different load eccentricities. The encasement of ECC improved the strength and ductility of columns. Li et al. [37] experimentally studied the behavior of PP-ECC and hybrid normal strength concrete (NSC) – ECC columns. They confirmed that the hybrid column showed higher deformability compared to an NSC column. In addition, the confining effect from the high tensile strength of ECC led to an overall increase in stiffness and peak strength of the columns.

A review of the existing research results highlights the lack of necessary behavioral aspects of a new composite combination between SHCC and concrete. That is a prefabricated concrete−filled SHCC tubular (CFPSHT) column. To the best knowledge of the authors, the previous literature has focused on the behavior of similar columns under concentric and cyclic loading. However, in structural applications, most of the columns are subjected to eccentric compression, and absolute concentric loading columns hardly exist. The new CFPSHT sheds light on the possibility of incorporating a high compressive and tensile strength cementitious material such as SHCC as a prefabricated tube that can bear axial load as well as serve as a confinement technique for the inner concrete core in a concrete filled−tubular column. Hence, this research was intended to bridge some of the performance gap information in the field of concrete−filled tubular (CFT) column structures, especially the use of advanced strain−hardening cementitious composites for producing a new kind of CFT column.

In this paper, the behavior of the proposed CFPSHT columns was studied experimentally and numerically. Firstly, eight columns were tested under eccentric loading, and the effects of using SHCC tubes with concrete and the load eccentricity on the behavior of CFPSHT columns were investigated. Secondly, based on the constitutive models of SHCC, concrete, and steel, the sectional load−moment capacity equations were derived and verified with the experimental results. Moreover, a refined finite element model (FEM) taking the effect of eccentricity on the confinement of the PSHCC tube in CFPSHT columns was developed to simulate the behavior of these columns. The accuracies of the FEM were validated against the experimental results. Finally, since the thickness of the SHCC tube and concrete core strength represent a vital role in construction efficiency and cost, it was significant to study their influences on the load−moment (P−M) interaction curves of the CFPSHT columns through a parametric study.

2. Experimental program

2.1. Test specimens

A total of eight square specimens were constructed and tested under eccentric loading. The specimen height (h) and cross−section width (b) were 1200 mm and 200 mm, respectively. According to ACI 318–19 [38] stipulations, the columns were classified as short columns, where the slenderness ratio ($\lambda = 20$) does not exceed 22 ($\lambda = kh/r$, where k = the effective length factor set to be 1.0 for pinned−pinned end condition in the test, h = the unsupported height of the column, r = radius of gyration and equals 0.30 b for square cross−sections), which showed that the second order effect could be ignored. All specimens were reinforced with four−deformed 12−mm bars as the longitudinal reinforcement and the lateral reinforcement was taken of steel ties with a 6−mm plain bar at a center−to−center spacing of 150 mm in the middle third. The steel ties were taken with a spacing of 50 mm at the column ends to prevent premature failure.

The specimens were divided into four conventional concrete specimens (C) as reference specimens and four CFPSHT specimens consisting of a PSHCC tube and concrete core (SH–C). Six specimens were tested as columns under eccentricity (e) of 0, 25, or 50 mm corresponding to eccentricity ratios of $e/b = 0$, 0.125 (relatively small eccentricity ratio), or 0.25 (relatively large eccentricity ratio), where b is the cross-section width. In addition to the columns, two specimens were tested as beams under pure bending, i.e. (e/b= infinity). It is worth mentioning that the SHCC tube thickness was 35 mm to ensure sufficient cover for reinforcing steel and flowability of SHCC owing to the congestion of reinforcement; otherwise, thinner thickness may compromise the pouring of SHCC. The specimen nomenclature indicated the type of the column and the eccentricity ratio. For instance, SH–C–0 indicates a CFPSHT column with an eccentricity ratio of zero. The specimens' details are summarized in Table 1, and the schematic structure of the specimens is shown in Fig. 1.

2.2. Materials properties

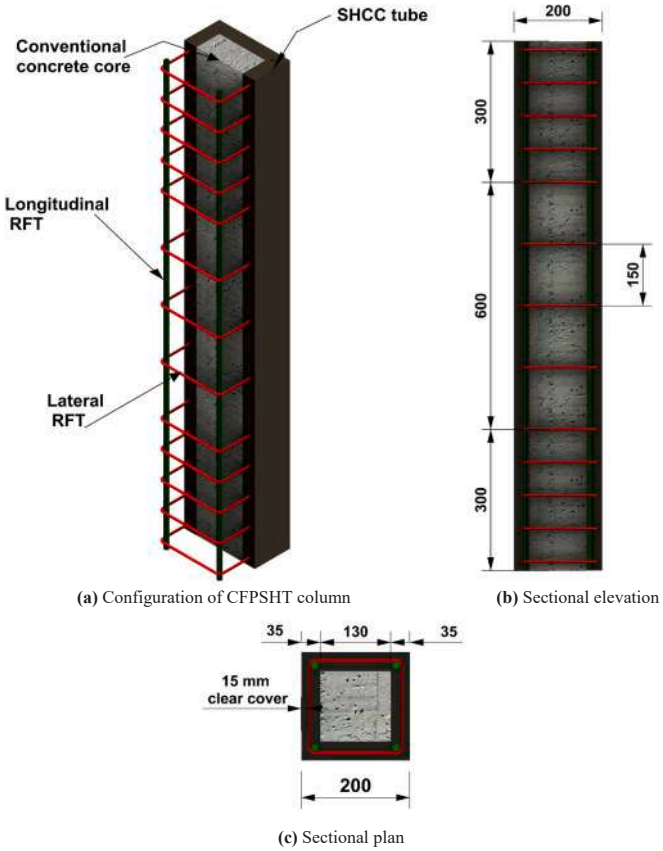
In the present study, conventional concrete was selected for comparison with SHCC to assess the effect of a prefabricated SHCC tube filled with conventional concrete in a CFPSHT column. SHCC and conventional concrete mixtures are given in Table 2. Ordinary Portland cement type I grade 42.5 with a specific gravity of 3.28, quartz sand with a fineness modulus of 2.4, silica fume with a specific surface area of more than 20000 m^2/kg, and polyproblyn (PP) fibers were the main components of the SHCC mixture. The diameter of the used PP fiber was 25 μm, length was 12 mm, volume fraction was 2 %, and nominal strength and Young's modulus were 2900 MPa and 116 GPa, respectively. The water−binder ratio was set as 0.20. Proper flowability of the SHCC matrix was ensured by adding a superplasticizer with the amount of 0.5 % binder content by weight. For the conventional concrete mixture, a nominal maximum size of 20 mm coarse aggregate, and a water–to–cement (w/c) ratio of 0.5 were used.

Material tests were conducted before testing the specimens. Direct uniaxial tensile tests obtained the tensile properties of the SHCC. According to the recommendation by Kunida et al. [27], Three specimens with a cross−section of 50 × 200 mm and a length of 900 mm were loaded using a displacement−controlled system at a loading rate of 0.005 mm/s. Specimen dimensions and test setup along with the typical tensile stress−strain curve are shown in Fig. 2, where the tensile stress−strain curve is marked by the pseudo strain hardening phenomenon. The average initial cracking strain and the average initial cracking stress were 0.013 % and 3.95 MPa, respectively, while the mean ultimate tensile strength was 6.30 MPa. Six cylinders with a diameter of 50 mm and a height of 100 mm, as recommended by JSCE [39] and Yu et al.

Table 1
Summary of tested specimens information.

Specimen designation	e (mm)	e/b	Longitudinal reinforcement (mm)	Lateral reinforcement (mm)	Type
C–0	0	0.00	4 Ø 12	Ø6@150	Conventional concrete
C–0.125	25	0.125	4 Ø 12	Ø 6@150	Conventional concrete
C–0.25	50	0.25	4 Ø 12	Ø 6@150	Conventional concrete
C–B	B	B	4 Ø 12	Ø 6@150	Conventional concrete
SH–C–0	0	0.00	4 Ø 12	Ø 6@150	CFPSHT
SH–C–0.125	25	0.125	4 Ø 12	Ø 6@150	CFPSHT
SH–C–0.25	50	0.25	4 Ø 12	Ø 6@150	CFPSHT
SH–C–B	B	B	4 Ø 12	Ø 6@150	CFPSHT

e = eccentricity; b = the cross– section width of the speciemens; e/b = eccentricity ratio; B: Eccentricity of infinity (the specimen was tested under four–point bending); CFPSHT: Concrete filled prefabricated strain– hardening cementitious composite tube.



(a) Configuration of CFPSHT column **(b)** Sectional elevation

(c) Sectional plan

Fig. 1. Structure of the CFPSHT specimens (Unit: mm).

[16,40], were loaded to extract their compression parameters at the same time as testing the specimens. The average compressive strength of SHCC was 53 MPa and the corresponding compressive strain was 0.38 %. The elastic modulus was 19 GPa. In addition, three concrete cylinder specimens with a diameter of 100 mm and height of 200 mm were also cast and tested simultaneously. The average compressive strength was 20.80 MPa, the corresponding compressive strain was 0.28 %, and the elastic modulus was 22 GPa. The uniaxial tensile tests were also conducted for the steel reinforcement, and the material properties are depicted in Table 3.

2.3. Specimen fabrication

The construction process of specimens was carried out in the laboratory. Steel cages and formworks were prepared as follows: steel ties and longitudinal bars were assembled to form a steel cage Fig. 3(a). The outer formwork was made of high–precision steel molds with one part of the same height as the tube and the other part was divided into three pieces to be fixed during casting Fig. 3(b). The steel cage was fixed within the inner formwork which was wrapped with a commercially available foam to facilitate demolding and ensure a rough surface of the inner interface of the SHCC tube. All the molds and steel cage were vertically fixed to a solid base to ensure that there was no movement of the molds and that the tube had a consistent thickness, Fig. 3(c).

Fig. 4 shows the casting of the PSHCC tube and the CFPSHT column. By considering the thin thickness of the SHCC tube and the dense reinforcement, it was crucial to cast SHCC properly without honeycombing. Hence, the SHCC was poured with three equal parts along the height of the specimen. After two days of curing, the formworks were removed to obtain the prefabricated SHCC tube. The tubes were cured in a water tank for two months before casting the concrete core to reduce the higher shrinkage and volumetric changes of SHCC, and to ensure a good bond between the interface of SHCC and concrete [41]. Finally, the concrete core was filled in the hollow SHCC tube in three equal layers and vibrated by a vibrating rod. The specimens were cured for 28 days before preparation for the test. The column ends were wrapped with two layers of carbon fiber reinforced polymer (CFRP) width of 100 mm to avoid potential local damage during the test.

It is worth mentioning that for real–world construction applications, the commonly used spinning process [42] could facilitate the efficient fabrication of the novel prefabricated SHCC (PSHCC) tube in specialized precast factories. This technique would use pre–designed, quickly assembled and disassembled inner and outer steel molds. The molds would rotate vertically along their longitudinal axis during the pouring process of SHCC, ensuring even SHCC distribution and consistent wall thickness throughout the tube. After that, the PSHCC could be transported to the site to act as a ready formwork, and the inner concrete core would be poured within it along with the cast of foundations. This could accelerate construction and reduce labor cost.

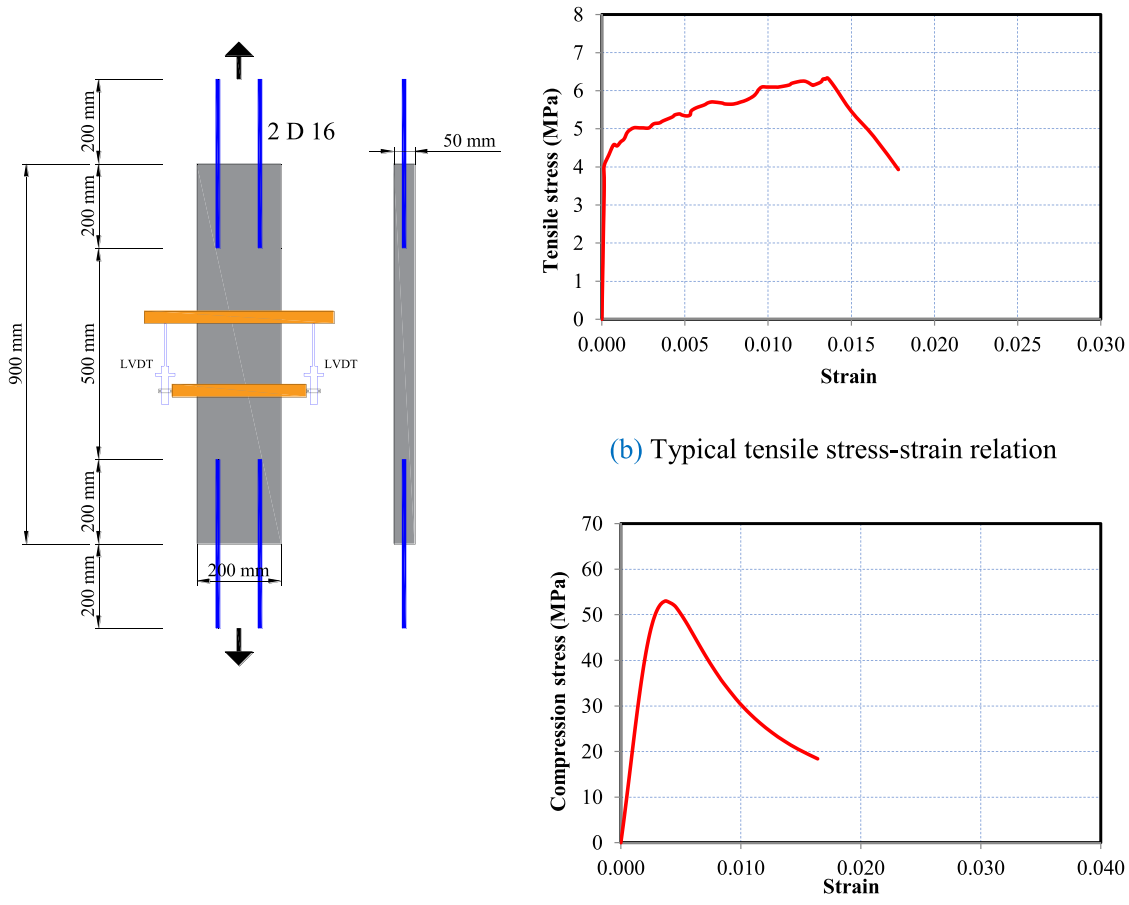
2.4. Test setup and instrumentation

The column specimens were tested under compression with different load eccentricities. A testing machine with a load of 2000 kN was used. The test setup for the specimens is shown in Fig. 5. Two pin supports positioned at the top and bottom of the specimens applied the load

Table 2
Mixture proportions (kg/m^3).

Mixture designation	W/B	Cement	Sand	Coarse pink limestone	Water	Silica fume	Super-plasticizer	Fiber (Volumetric ratio %)
Concrete	0.50	300	650	1130	150	—	—	—
SHCC	0.20	1243	149	—	293	223	7.33	16.20 (2 %)

SHCC = Strain–Hardening Cementitious Composites; W/B = water/ binder ratio, B = Binder (cement + silica fume).



(a) Typical setup of a tensile specimen

(b) Typical tensile stress-strain relation

(c) Compressive stress-strain relation

Fig. 2. Dimensions of the axial tensile test specimen and typical stress-strain relationships of SHCC.

Table 3
Material properties.

Parameter	Specimen description and dimensions	Average value
Average compressive strength of concrete, f_c'	3 cylinders Ø100 × 200 mm	20.80 MPa
Average compressive strength of SHCC, f_{SHCC}'	6 cylinders Ø50 × 100 mm [16,39, 40]	53.00 MPa
Average ultimate tensile strength of SHCC, f_{tu}	50 × 200 × 900 mm [27]	6.30 MPa
Yield strength of the longitudinal bars, f_{yl}	————	402 MPa
Yield strength of steel tie, f_{yt}	————	240 MPa

eccentricity (e). The bearing plates were 50 mm thick and 260 mm in breadth, while the cylinder rod was 50 mm in diameter. This configuration allowed for free rotation of specimen top and bottom surfaces due to eccentric loading.

The specimens were instrumented internally and externally. The result of axial deformation was recorded by linear interpolating the readings of two Linear Variable Differential Transformers (LVDTs) L_1 and L_2 attached to the upper loading head attached to the column. For eccentrically loaded columns, in addition to the axial deformation, the lateral displacement of the columns was measured using three horizontal LVDTs (L_3, L_4, and L_5). The strains in the reinforcement were measured through strain gauges (S_1 and S_2) attached at the mid−height of the lateral ties and mid−height of the longitudinal bar. Specimens were preloaded up to 5 % of the estimated ultimate capacity of columns to prevent minor movements between the loading heads and the specimen. The axial load, axial deformation, lateral deformation, and strains were gathered using a data acquisition system.

For the beam specimens, Steel plates were used where the top plates have a span of 340 mm, while the bottom plates have a span of 1100 mm. Three LVDTs (L_1, L_2, and L_3) were used to measure the deflection of the beam.

3. Test results and discussion

3.1. Mode of failure and crack pattern

The crack pattern of the tested specimens represents the distribution of cracks during the failure process, which provides useful information regarding the failure mechanism of the columns.

The propagation of failure for the specimens is shown in Fig. 6. For the column specimens, the first visual crack was observed around the middle third of all specimens. However, the conventional concrete columns failed in a completely different manner compared to CFPSHT columns under both concentric (e/b= 0) and eccentric loading (e/b= 0.125 or 0.25). For the reference conventional concrete column C–0, the first crack was observed at about 75 % of the ultimate load. After the first crack occurred along the corner of the column due to high stress concentration, wide cracks developed throughout the column surface until the mid-height concrete crushed suddenly and the cover spalled off explosively with a loud noise. Consequently, the bar buckling was evident at the region of failure indicating a brittle failure mode; see Fig. 6(a). On the other hand, the PSHCC tube experienced tensile stress due to the lateral expansion of the inner concrete core in the CFPSHT

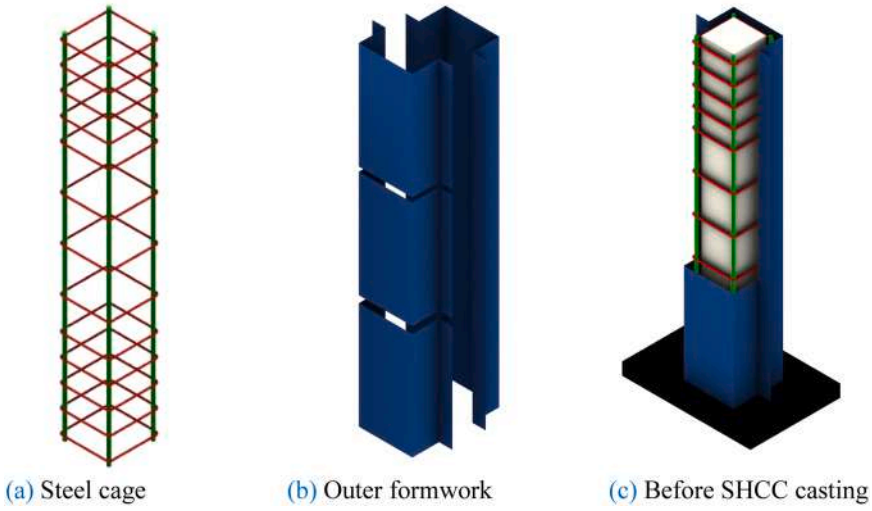


Fig. 3. Preparations for casting the PSHCC tube.

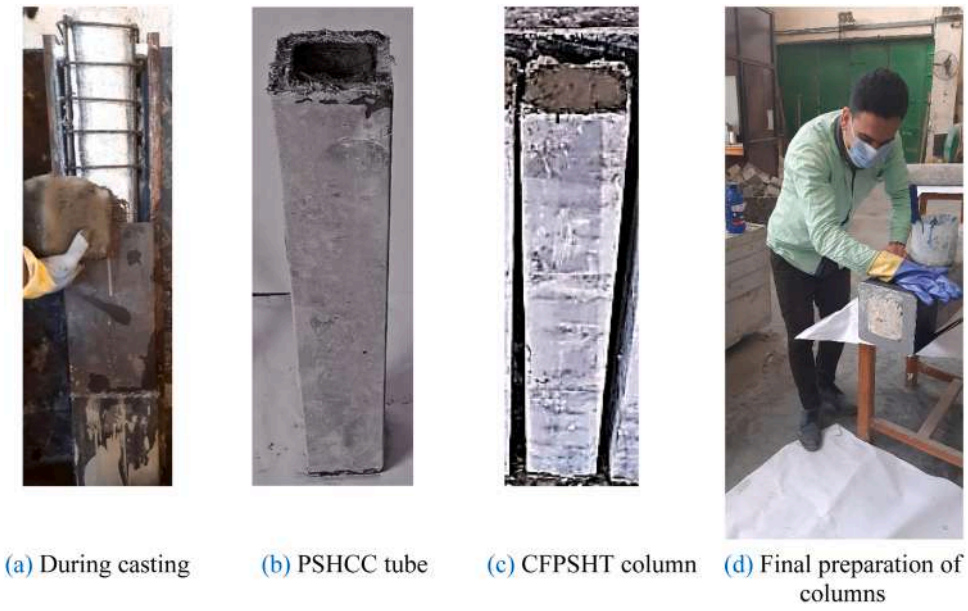


Fig. 4. The Casting process and the final CFPSHT column.

column SH-0. This resulted in small visible hairline cracks at the surface of the column at approximately 45 % of the ultimate load. Owing to the high tensile deformability of SHCC, it could sustain high lateral expansion and keep the width of cracks greatly reduced compared to concrete, which leads to increased durability. After initial cracking, micro–cracks developed throughout the specimen due to the crack ability of SHCC. Prior to the ultimate load, a vertical wide crack occurred at the corner of the column with a loud noise resulting from the tensile rupture of PP fibers, indicating SHCC splitting. However, the cover remained attached until the end of testing. This can be attributed to the fiber–bridging effect in the SHCC material. A close investigation after the cover was removed manually revealed the core concrete to have severe damage, the lateral tie was slightly opened, and the bar buckling was deferred as shown in Fig. 6(b). This indicates that SHCC can achieve high confinement to the inner core and the longitudinal bars compared to conventional concrete. It is worth noting that, part of the concrete was attached to the concrete indicating a full bond between the PSHCC tube and the concrete core.

For columns tested under e/b= 0.125 or 0.25, the conventional concrete columns, C–0.125 and C–0.25 suffered concrete crushing and bar buckling on the compression side, as clarified in Fig. 6(c) and 6 (e). The first vertical crack was noticed near the mid–height of the column and at approximately 58 % and 32 % of their ultimate loads for C-0.125 and C-0.25, respectively. Upon failure, the concrete cover spalled, and the longitudinal bars were severely buckled. On the tension side, it was found from the test observations that the cracks initiated on the tension side and extended towards the far side. The crack width increased directly with the applied load until it became visible and wider at failure. The crack width was observed to be as wide as 2 mm up to failure in case of 50 mm eccentricity.

Fig. 6(d) and 6 (f) show that the existence of the PSHCC tube made the failure pattern different for the CFPSHT. Initially, Tiny and distributed cracks occurred in both compression and tension faces of the columns at about 49 % and 30 % of the ultimate loads for SH–C–0.125 and SH–C–0.25, respectively. With the increasing load, flexural tension cracks propagated along the height of the columns. On the compression face, SH–C–0.125 and SH–C–0.25 suffered distributed cracks, followed by delayed buckling of longitudinal reinforcement. The bar buckling

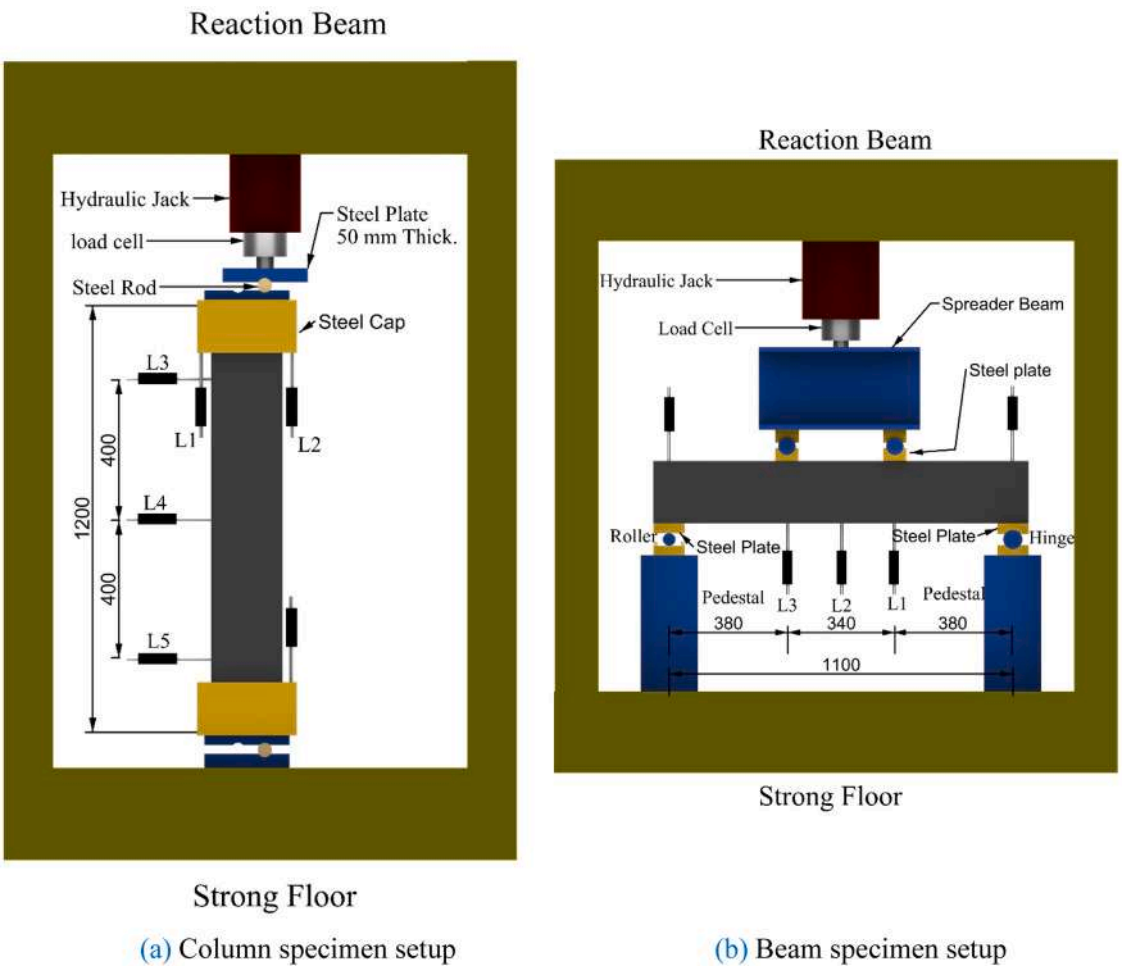


Fig. 5. Test setup for specimens (Unit: mm).

was greatly deferred on the compression side compared to conventional concrete columns. This is attributed to the fiber bridging effect, which can achieve high confinement to the longitudinal bars. With the increasing load, the existing cracks widened, and some visible flexural tension cracks propagated along the height of the columns. At the ultimate load, specimens failed gradually due to the oversized tensile cracks, and the SHCC in the compression side reached its ultimate strain, however, remained slightly uncrushed, which was different from concrete columns. At the failure stage, it can be observed that longitudinal bars were buckled and wide cracks formed, followed by hearing a loud sound at the compression face indicating some splitting of SHCC. However, the outer SHCC did not spall, and the column maintained its integrity. This can be attributed to the PP fiber bridging effect. On the tension side, dozens of tiny cracks with a small crack spacing and a maximum crack width of 0.4 mm were observed before the final failure of the CFPSHT columns. The fine cracks for columns containing SHCC tubes are due to SHCC's superior tensile deformability. It was also observed that the fine cracks in the tension side for column SH–C–0.125 were numerous and converged to main cracks, and at failure, a hissing sound was heard indicating pulling out of PP fibers. It can be concluded from the previous observations that replacing the outer concrete with a PSHCC tube reduces the crack width, which leads to columns being more durable.

For the beam Specimens, the first flexural crack appeared at the tension side. After the first crack, as the load increased, new cracks developed between the loading points and along the shear span. In contrast, the existing cracks propagated towards the compression side of the specimens. For concrete beams, with further increased load, the cracks within the shear span propagated towards the loading point. Concrete cover spalling started at the compression side at mid−span. Although the CFPSHT beam showed similar behavior until failure, the cracks were much increased in number and tinier. The SHCC exhibited gradual crushing at the compression side. Afterward, the specimen could sustain increased load according to the high compressive strain and deformation of SHCC, and excessive deformation with wider flexural cracks was visible until the outmost bar in tension was about to rupture.

3.2. *Load versus deformation curves*

The relationship between the axial load and the axial displacement is given in Fig. 7 for tested columns. Table 4 reported the main experimental results of columns, including the ultimate load and its corresponding vertical displacement and mid–height lateral displacement. For reference conventional concrete columns, the curves followed almost a straight line till reaching the ultimate load, then dropped suddenly under concentric loading, while the drop in load was flattened and more gradual under eccentric loading. The curves for CFPSHT columns showed more deformability for both concentric and eccentric loading. This can be explained as, for the CFPSHT columns, during the initial stage, both the concrete core and the SHCC tube can bear load simultaneously. The concrete core began to lose its load sharing until reaching its maximum strain. The outer SHCC tube was confining the inner core at this deformation, which increased the deformation capacity. It was noticed that the ultimate loads for CFPSHT columns were much higher than their corresponding reference conventional concrete columns, owing to the superior compressive strength of SHCC as well as

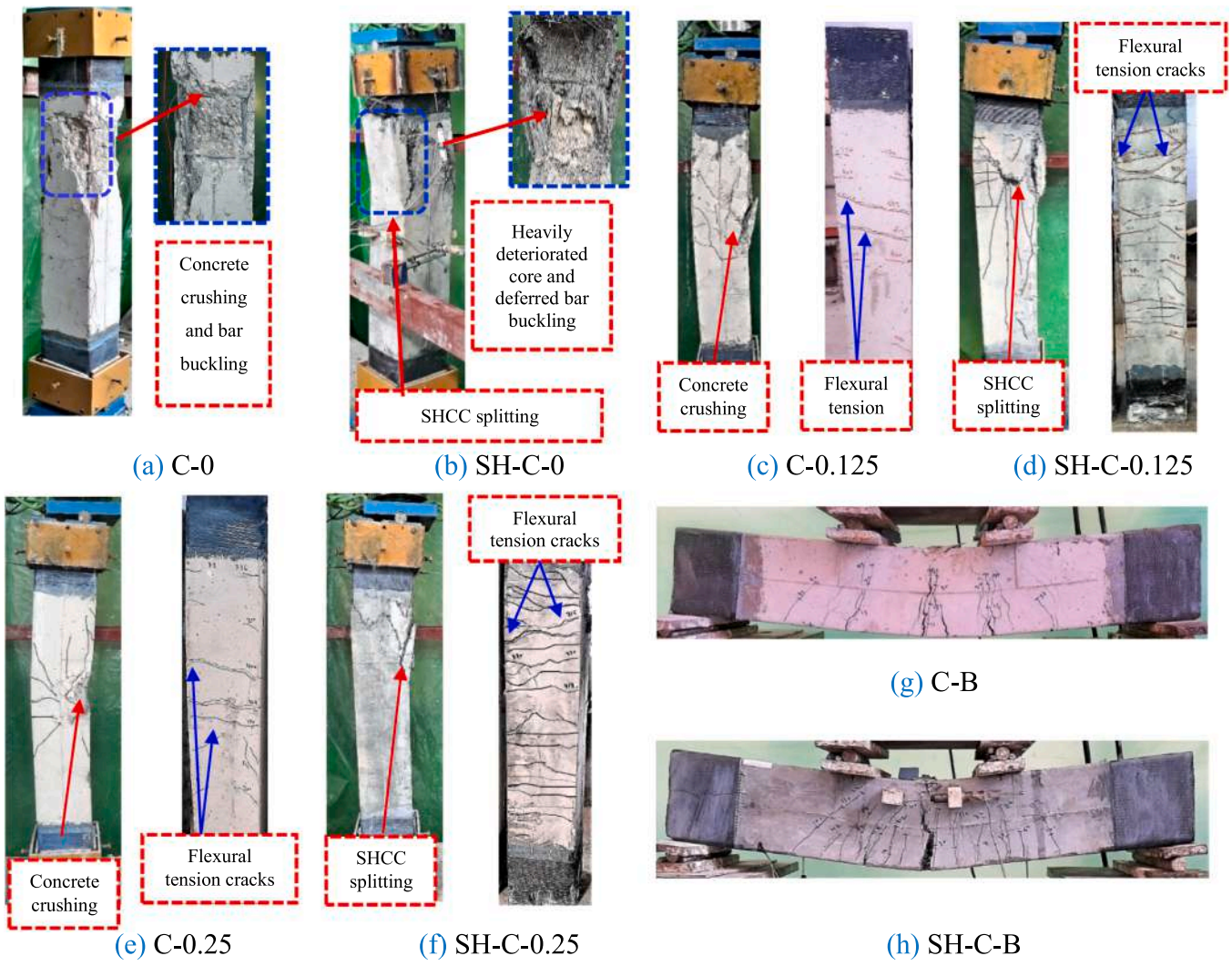


Fig. 6. Mode of failure of all specimens.

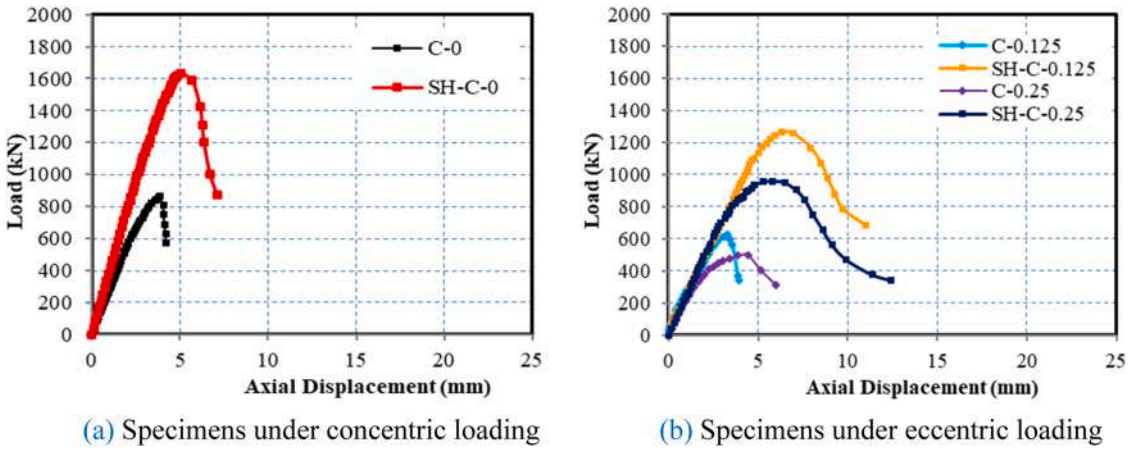


Fig. 7. Axial load vs axial displacement curves for column specimens.

the deformability of SHCC, which allowed the PSHCC tube to give high confinement for the concrete core. Similarly, the load mid–span deflection for the specimens tested under four–point bending is shown in Fig. 8. The maximum load was increased by 63 % for the composite beams, and the deformation increased by 20 % as well.

The lateral displacement behavior of columns showed a similar response to the axial displacement behavior, as shown in Fig. 9. The displacement increased linearly until the peak load was reached. Hereafter, the displacement increased at a faster rate with decreased axial load in conventional concrete columns, while the lateral displacement

Table 4
Key characteristic points for columns.

Specimen	P_{cr} (kN)	P_u (kN)	Δ_u (mm)	Δ_y (mm)	$\Delta_{0.85}$ (mm)	Δ_{Lu} (mm)	$\Delta_{0.85}$ (mm)	P_{cr}/P_u	$\Delta_{0.85}/\Delta_y$	$\Delta L_{0.85}/\Delta l_u$
C–0	660	869	3.89	3.28	4.10	0.00	0.00	0.75	1.25	0.00
C–0.125	368	628	3.60	3.38	3.86	2.30	2.58	0.58	1.14	1.12
C–0.25	160	498	4.44	3.68	4.64	3.45	4.30	0.32	1.26	1.25
C–B	18	65	—	4.32	14.38	—	—	0.27	3.32	—
SH–C–0	819	1630	5.05	4.42	6.27	0.00	0.00	0.47	1.42	0.00
SH–C–0.125	619	1265	6.15	5.36	8.50	3.69	6.97	0.49	1.59	1.89
SH–C–0.25	291	970	5.16	4.23	7.60	4.25	8.43	0.30	1.79	1.98
SH–C–B	26	97	—	5.47	33.00	—	—	0.27	6.03	—

P_{cr} = the cracking load; P_u = the ultimate load; Δ_u, Δ_{Lu} = the corresponding axial and lateral displacement to the ultimate load, respectively; $\Delta_{0.85}$and $\Delta L_{0.85}$= the corresponding axial and lateral displacements to 85 % of the ultimate load in the softening branch in the load–displacement curve.

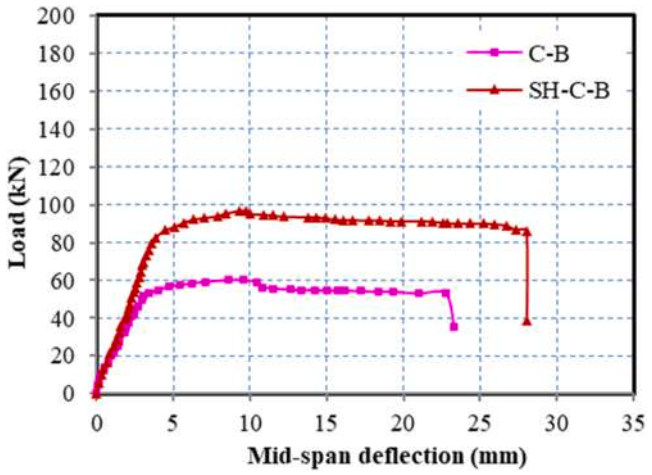


Fig. 8. Load-mid span deflection diagrams for beam specimens.

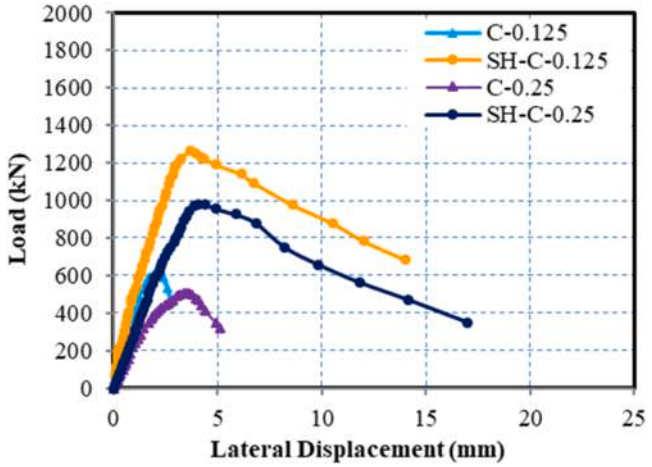


Fig. 9. Axial load vs lateral displacement curves for column specimens.

decreased slightly after the peak load for the CFPSHT columns until failure owing to the tensile ductility of SHCC, which increases the ductility of columns under eccentric load. A remarkable decrease in stiffness was observed when the eccentricity increased to 50 mm. This is reasonable since as the eccentricity increases, a higher moment is induced.

3.3. Ductility and key characteristics

The key behavior characteristics of the specimens based on the above load–deformation behavior are given in Table 4, which are the cracking load, P_{cr}, the ultimate load, P_u, and its corresponding axial and lateral displacement (Δ_u and Δ_{Lu}), and $P_{0.85}$ which is defined as the load when the ultimate load drops by 15 %. i.e., $P_{0.85} = 0.85P_u$ [43] and its corresponding axial and lateral displacements ($\Delta_{0.85}$ and $\Delta_{L0.85}$), as well as the ductility index as an explicit indication to quantify the post–peak behavior of the specimens. As shown in Fig. 10, the ductility index D.I. proposed by Hadi et al. [43] was adopted in this study. D.I. is defined as the ratio of the displacement at 85 % of the ultimate axial load in the softening part of the axial load axial displacement curves and the axial displacement at yield load in the hardening part of the curve, i.e., $D.I. = \Delta_{0.85}/\Delta_y$. Compared to the reference conventional concrete columns, the ductility index for CFPSHT specimens was enhanced in all cases. Precisely, the ductility index for SH-0 was improved by 13.60 % more than its reference column C–0. For columns under eccentric loading, the improvements in ductility index were 39.40 % and 42 % for SH–C–0.125 and SH–C–0.25 in correspondence with their reference specimens C–0.125 and C–0.25, respectively. The improvements in ductility index can be attributed to the ability of the PSHCC tube to not only increase the ultimate loads of columns but also the confinement of the concrete core, which in turn increases the ultimate displacements of columns; refer to Table 4. As for columns tested under eccentricity ratios

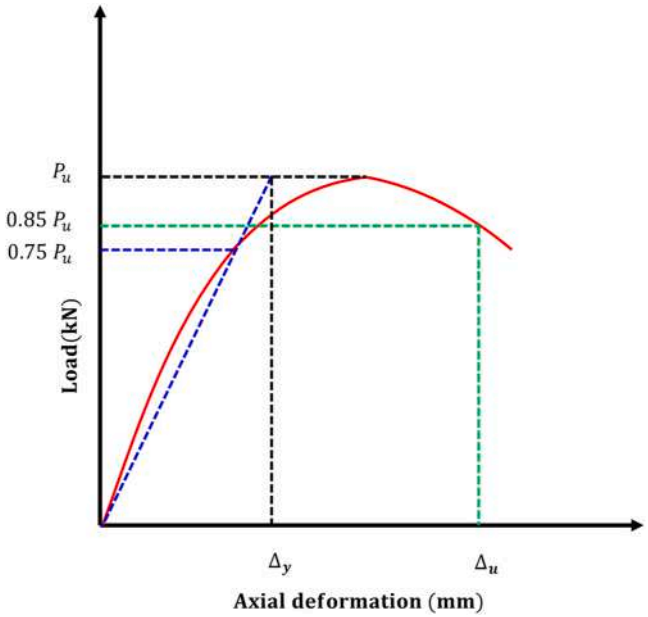


Fig. 10. Definition of the yield and ultimate deformations, Hadi et al. [43].

of 0.125 and 0.25, the ratio of $\Delta_{L0.85}/\Delta_{Lu}$, at the middle section, reflects the deformability of the columns. The lateral deformation has been enhanced due to the good confinement of the PSHCC tube and the tensile ductility of SHCC. The enhancement was 89 % for an eccentricity ratio of 0.125 for the CFPSHT column, compared to only 12 % for an eccentricity ratio of 0.125 for the corresponding conventional column.

The ratio of P_{cr}/P_u reflects the crack resistance. It can be noted that the CFPSHT columns (0.30–0.47) seem to be easier to crack than the conventional columns (0.32–0.76). This can be caused by the tensile characteristics of the SHCC material, which exhibits multiple cracking stages before complete failure. This means that it reaches a lower initial cracking load because it accommodates deformation through microcracking rather than forming a single localized crack as conventional concrete exhibits. For instance, the cracking load appeared at 76 % of the ultimate load for conventional concrete column C–0 while appeared at 47 % for the CFPSHT column SH–C–0. Similar observations were established by Zhang et al. [44]. The ultimate load increased dramatically using the SHCC tube compared to the conventional columns owing to the high compressive strength and confinement of the PSHCC tube. The ultimate load increased by 88 % under concentric loading, while it increased by 101 % and 94 % in the cases of $e/b = 0.125$ and 0.25, respectively.

3.4. Strain Analysis

The strain profile of the outmost longitudinal bar in tension is shown in Fig. 11. The horizontal axis represents the strain recorded by the strain gauge, and the vertical axis represents the axial load. The positive sign of strain represents the tensile strain, while the negative sign represents the compressive strain. When the eccentricity is small, i.e., (e = 25 mm), the full cross–section of specimen C–0.125 is in compression, and the measured value at the outmost steel bar in tension was −230 με at the ultimate axial load. After reaching the ultimate load, the concrete cover spalled, the stiffness was reduced, and more bending stress in both tension and compression faces was induced. Consequently, the strain in the outmost tension bar changed from compression to tension and then progressively increased. On the other hand, for CFPSHT specimen SH–C–0.125, the strain of the outmost tension bar remained in compression in a steady state, and the strain value was −690 $\mu\varepsilon$. When tested under a relatively large eccentricity, i.e. ($e = 50$ mm), a small part of the cross–section was under tension, and the strain of the outmost tension bar was tension for both the conventional concrete column and the CFPSHT column strains at the peak load were 2152 and 1317 $\mu\varepsilon$ for C–0.25 and SH–C–0.25, respectively.

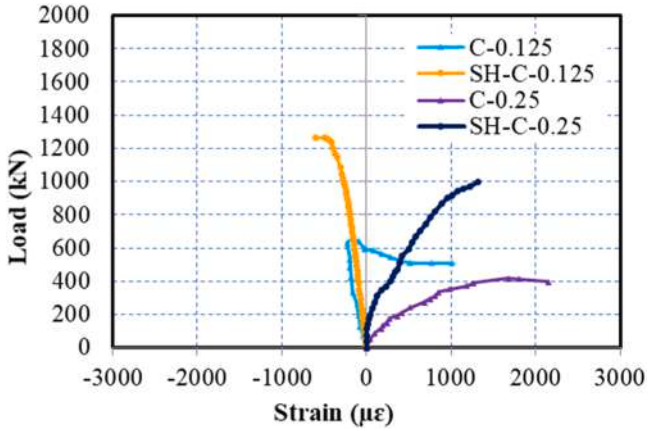


Fig. 11. Strain profiles of the outmost longitudinal bar in tension.

3.5. Experimental P–M interaction diagram for CFPSHT columns

Fig. 12 shows the load–Moment (P–M) diagrams that illustrate the relationship between axial load and bending moment capacities under various load eccentricity ratios for the columns. Each diagram consists of four points representing specific column conditions and capacities. The first point on the curve represents columns tested under pure compression without any bending moment. It assumes the entire concrete section is experiencing pure compression, with the axial force values given in Table 4. The second and third points correspond to the columns' axial load–carrying capacity, with the accompanying moment capacity represented on the horizontal axis. These moment capacities, listed in Table 5, are calculated by multiplying the ultimate axial load (P_u) with the total eccentricity ($e + \Delta l$), where e is the load eccentricity and Δl is the lateral deformation at ultimate resistance at the ultimate load measured by transducer L4, refer to Fig. 5(a), to incorporate secondary moments. The fourth point represents columns tested under pure bending without any axial force. The moment capacity at this point is calculated by multiplying the support reaction (half the applied ultimate load in the four–point flexural test, as shown in Fig. 5(b)) with the distance from the support to the point load.

The results indicate that using reinforced SHCC tubes has a positive effect on the column's ability to resist bending moments, particularly at the maximum loading eccentricity ratio investigated ($e/b = 0.25$). It should be noted that this study in the experimental program did not explore strength improvement beyond $e/b = 0.25$ except for the pure bending case which represents a tension–controlled failure. Nevertheless, it is expected that the enhanced strength could still be achieved even when compression is not the dominant failure mode in the columns, as the SHCC exhibits both higher compressive and tensile strengths in comparison with conventional concrete.

4. Analytical Modeling

The P–M interaction diagram was computed using a detailed section analysis based on strain compatibility, internal force equilibrium, and the controlling strength limit state. The cross–section analysis was performed based on the assumptions of plane sections remain plane after deformation, a perfect bond between steel and the SHCC, and concrete, SHCC, and the factor of safety for materials was set to unity. The material stress–strain behaviors were simplified; as elastic perfectly plastic behavior is assumed for the stress–strain behavior of steel. The behavior of concrete and SHCC in compression was similarly simplified to an equivalent stress block. However, in tension, the behavior of concrete can be neglected. On the other hand, the tensile stress of SHCC should be

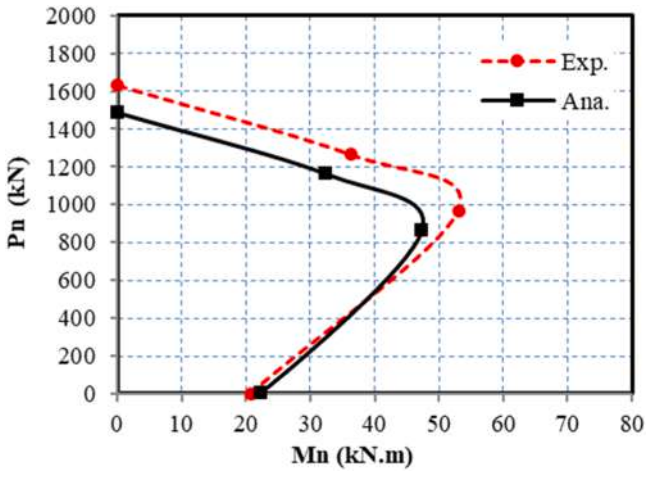


Fig. 12. Experimental and analytical interaction diagram for CFPSHT specimens.

Table 5
Comparison between experimental and analytical calculations of load and moment capacities of CFPSHT columns.

Specimen	Eccentricity (mm)	Experimental Calculations		Analytical Calculations		$P_{u,Exp}/P_{u,Ana}$	$M_{u,Exp}/M_{u,Ana}$
		$P_{u,Exp}$ (kN)	$M_{u,Exp}$ (kN.m)	$P_{u,Ana}$ (kN)	$M_{u,Ana}$ (kN.m)		
SH−C−0	0 mm	1630	0.00	1488.00	0.00	1.10	NA
SH−C−0.125	25 mm	1265	36.29	1150.77	33.00	1.10	1.10
SH−C−0.25	50 mm	970	53.01	864.20	47.27	1.13	1.13
SH−C−B	Infinite	0	20.74	0.00	21.53	NA	0.97

$P_{u,Exp}$ = the experimental ultimate load; $M_{u,Exp}$ = the corresponding experimental moment capacity; $P_{u,Ana}$ = the analytical ultimate load; $M_{u,Ana}$ = the corresponding analytical moment capacity; NA = not applicable.

considered owing to its higher ductility and tensile strength [39,45]. To simplify calculations, The SHCC material in the tension region was assumed to have an equivalent block of f_{tu} (The tensile strength of SHCC). The simplified stress–strain curves of materials are shown in Fig. 13 where the constitutive model of confined concrete in this paper follows the assumptions of Popvics [46] and Mander [47].

The compressive stress–strain curve of the confined concrete can be derived from the models provided by Popvics [46]:

$$\frac{\sigma_c}{f'_{cc}} = \frac{\left(\frac{\varepsilon_c}{\varepsilon_{cc}}\right) r}{r - 1 + \left(\frac{\varepsilon_c}{\varepsilon_{cc}}\right)^r} \tag{1}$$

$$r = \frac{E_c}{E_c - \frac{f'_{cc}}{\varepsilon_{cc}}} \tag{2}$$

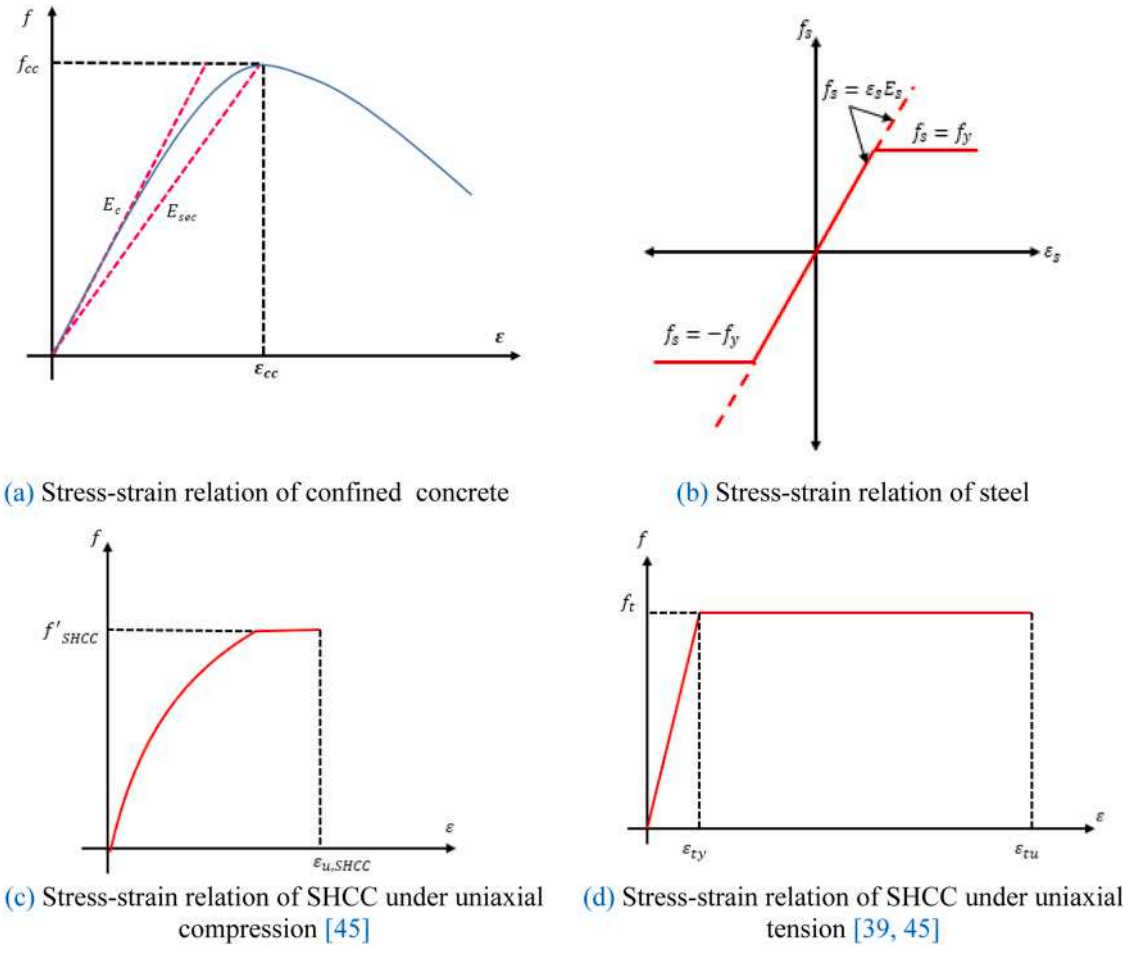
where, f'_{cc}, ε_{cc} are the compressive strength and corresponding strain of concrete under certain confining pressure, respectively. The strain corresponding to f'_{cc}, can be determined by the proposed equation by Mander [47] as the following:

$$\varepsilon_{cc} = \varepsilon^*{}_o \left[1 + 5\left(\frac{f'_{cc}}{f'_c} - 1\right)\right] \tag{3}$$

where, $\varepsilon^*{}_o$ donates the strain at f'_c. In Eqs. (1) and (3), f'_{cc} is defined by the model proposed by the authors [48] by regression analysis which was similar to the model proposed by Teng et al. [49], as follows:

$$f'_{cc} = f'_c + 4.52(f'_{l,t} + f'_{l,SH}) \tag{4}$$

where:



(a) Stress-strain relation of confined concrete

(b) Stress-strain relation of steel

(c) Stress-strain relation of SHCC under uniaxial compression [45]

(d) Stress-strain relation of SHCC under uniaxial tension [39, 45]

Fig. 13. Idealized stress-strain curves of materials.

$$f'_{l,SHCC} = k_s \frac{2f_{tu} \times t_{SHCC}}{b_c} \quad (5)$$

$$f'_{l,t.} = \frac{1}{2} k_e f_l \quad (6)$$

where, $f'_{l,SH}$ and $f'_{l,t.}$ are the effective lateral pressure of the SHCC tube and lateral ties, respectively, f_{tu} is the tensile strength of SHCC from the direct tensile test, t_{SHCC} is the thickness of the SHCC tube, b_c is the breadth of the concrete core, and k_s is the shape factor considering the confinement effectiveness for square CFPSHT columns and is given by the ratio of the effective confinement area to the total area of concrete enclosed by the SHCC tube and is adopted to be 0.33. f_l is the lateral pressure of lateral ties, given by Mander [47], and *ke* is the confinement effectiveness coefficient and can be calculated as follows:

$$k_e = \frac{\left(1 - \sum_{i=1}^{n} \frac{(w'_i)^2}{6b_s{}^2}\right)\left(1 - \frac{s'}{2b_s}\right)^2}{1 - \rho_{cc}} \quad (7)$$

where b_s is the width of the lateral ties between lateral tie bar centers, s is the spacing between the centerlines of lateral ties, s' is the clear vertical spacing between tie bars, w'_i is the clear spacing of longitudinal bars, and ρ_{cc} is the ratio of the area of longitudinal reinforcement to the area of the core of the section.

Under the previous assumptions, at any level of eccentric loading, the location of the neutral axis, the corresponding strain distribution, and the assumed stress distribution are shown in Fig. 14. Accordingly, the compressive force P_u can be calculated by summation of forces as follows:

$$P_u = F_{SH} + F_C + \sum_{i=1}^{n} F_{si} - F_t \quad (8)$$

The compression force of concrete, F_c, can be estimated based on the equivalent stress block, generally calculated as:

$$F_C = 0.85 f'_{cc} \times A_c \quad (9)$$

The compressive force of SHCC $F_{SH}$is the summation of SHCC area multiplied by the strength of SHCC (f'_{SH}) where:

$$f'_{SH} = \alpha_c f'_{SH,exp.} \quad (10)$$

The factor α is taken at 0.85 according to ACI 318–19 [38]. Also, $f'_{SH,exp.}$ is the cylinder compressive strength of SHCC from experimental testing. Additionally, the Area of SHCC is the summation of the areas as follows:

$$A_{SH1} = b_c \times t \quad (11)$$

$$A_{SH2} = (b - b)_c) \times a \quad (12)$$

t is the thickness of the SHCC tube, and the depth of the equivalent block (a) to the depth of the neutral axis (X_c) is defined as:

$$a = \beta_c \times X_c \quad (13)$$

Factor (β_c) should not exceed 0.85, but shall not be less than 0.65 [38]. It can be derived as:

$$\beta_c = 0.85 - [0.05(f'_{SH} - 28)/7)] \quad (14)$$

Conclusively,

$$F_{SH} = f'_{SH} \times (A_{SH1} + A_{SH2}) \quad (15)$$

The force in longitudinal steel at any layer is given by:

$$F_{si} = f_{si} \times A_{si} \quad (16)$$

Due to the excellent performance of SHCC in tension, its sharing portion in tension should be considered as follows:

$$F_t = f_{tu} \times A_{t,SH} \quad (17)$$

where, $A_{t,SH}$ is the areas of SHCC in the tension zone and calculated as $((b - b_c) \times t)$ and $(X_t \times t)$. X_t is the depth of the tension zone below the neutral axis.

Based on the equivalent stress block and equilibrium of forces, the corresponding moment M_n was calculated by summation of the moment of forces about the neutral axis for square CFSHT columns as follows:

$$M_u = F_{SH1} \times (0.5h - 0.5t) + F_{SH2} \times (0.5h - 0.5a) - F_C \times (0.5h - 0.5[0.85(X_c - t)] + F_{t1} \times [0.5(h - X_c)0.5h] + F_{t2} \times (0.5t - 0.5h) + \sum_{i=1}^{n} F_{si} \times [h - d_i - 0.5h] \quad (18)$$

Fig. 12 shows the developed interaction diagrams for the CFPSHT columns following the section analysis proposed method. The analytical axial and flexural capacities were less than the experimental results in most cases. Since the factor of safety for materials was set to unity and by further adopting the factor of safety for design in actual applications, a safe design could be ensured. Table 5 lists the experimental–to–analytical ratio of the ultimate axial and bending–moment

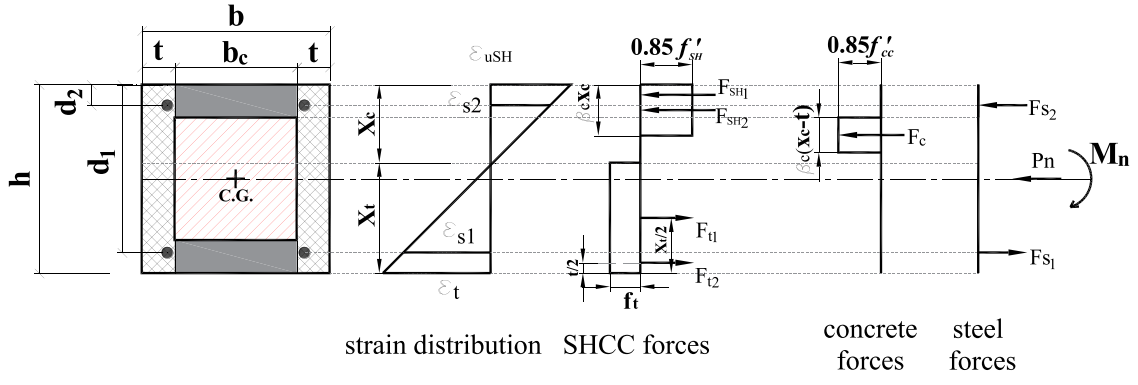


Fig. 14. Stress-Strain distribution for CFPSHT columns.

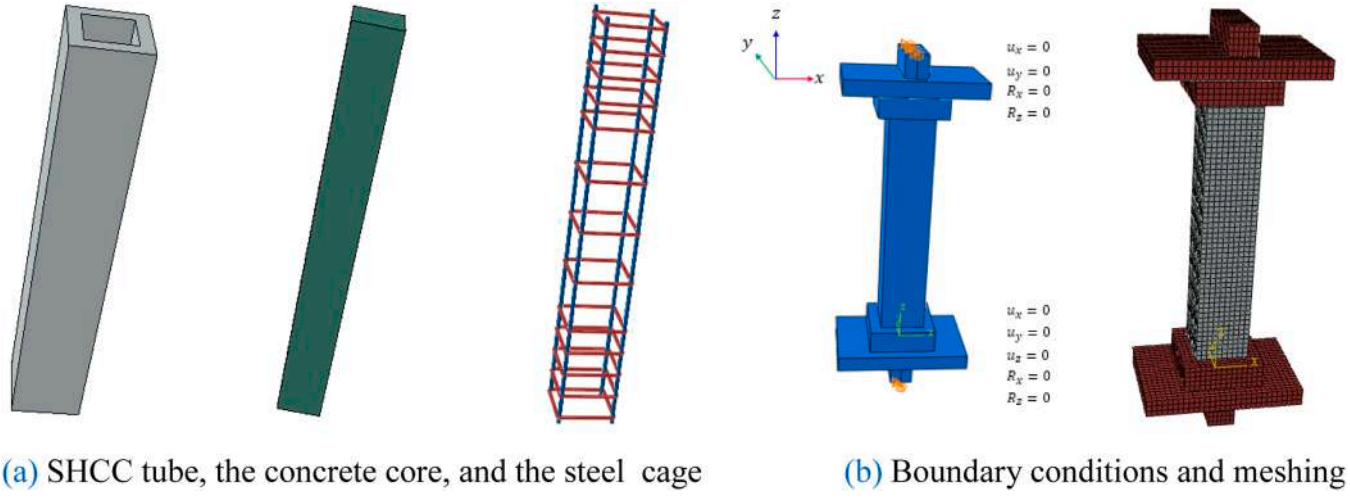


Fig. 15. Defined elements, boundary conditions, and meshing in ABAQUS.

capacities of the tested specimens.

5. Finite element modeling

5.1. Model overview

This study employs a finite element model (FEM) to investigate the influence of factors such as the eccentricity ratio, the concrete core strength, and the SHCC tube thickness on the eccentric compression behavior of the proposed CFPSHT composite columns by first validating the results of the experimental work.

The eccentric compression behavior of the CFPSHT in this study was investigated using ABAQUS [50]. As shown in Fig. 15 (a), the defined elements were the SHCC tube, the concrete core, and the steel reinforcements. ABAQUS solid element C3D8R was used for modeling both the SHCC tubes and the concrete core, which can be used for linear and complex nonlinear analysis involving contact, plasticity, and large deformations [51]. The steel reinforcements were modeled through truss elements with two nodes (T3D2). The steel reinforcements (truss elements) were embedded within the SHCC (solid elements), forming a perfect bond between these two materials. However, a slip between them was expected in reality, which is incorporated indirectly through the tension–stiffening feature of the concrete damage plasticity model (CDPM), which is the most advanced material model provided by ABAQUS for simulating cementitious materials. The contact between the concrete core and the SHCC tube was modeled using the Surface–to–Surface contact. Throughout the test, no separation was observed between the concrete core and the SHCC, indicating that they were in full bond. Coulomb friction and nominal hard contact were employed to simulate this contact behavior, and the friction coefficient was defined as 1.0, Tian et al. [52].

For accurate simulation, steel caps made of rectangular plates were employed at the ends of columns. These steel caps were modeled with 3D components (C3D8R) and an elastoplastic material model [53]. In addition, two additional steel plates were used at the two ends of the columns for loading application. All plates were aligned and centered. For eccentrically loaded columns, the positions of the loading lines were moved from the central line by the needed eccentricity. The contact between the steel cap and the column was ensured using ABAQUS's surface–to–surface contact algorithm considering a friction coefficient of 0.6 to account for the lateral confinement effect on the column caused by the steel rings, [52]. To connect the loading plate to the steel cap, a tie constraint was adopted.

In Fig. 15 (b), All translational displacements in the x, y, and z directions of the nodes laying on the center line at the loading plates were restrained except for the translation in the z direction for the top plate was kept free. The rotational about x and z directions was constrained at the top and bottom plates. Before executing the numerical analysis on the columns, a mesh sensitivity analysis was performed to determine the optimal mesh, with no noticeable change in results. Mesh sizes of 45, 35, 25, 15, and 5 mm were tested to determine the best fit. The model with a mesh size of 15 mm was selected because it yielded the most accurate results.

5.2. Material modeling

5.2.1. Concrete

The CDPM adopted in ABAQUS was used to simulate the materials. The CDMP represents the inelastic behavior of concrete with isotropic damage using isotropic compression/tension plasticity models. It adopts a yielding criterion illustrated in [54,55] to define the conditions under which concrete yields under a three–dimensional stress state. The plastic stress versus strain relationship is determined by assuming a non–associated potential plastic flow rule. The plasticity parameters in the CDPM, as given in Table 6, were: the ratio of the biaxial/ uniaxial compressive strength $\sigma_{b0}/\sigma_{c0} = 1.16$, the flow potential eccentricity $\varepsilon = 0.1$, the sahpe coefficient $K = 0.667$, as recommended by ABAQUS. The dilation angle of $\varphi = 32^{\circ}$ was iteratively calibrated to match the experimental test results. Besides, a small value for the viscosity parameter ($\mu = 0.0001$) is defined to improve the convergence rate in the concrete softening and stiffness degradation regimes, following the suggestion from Barth and Wu [56]. The two parameters needed to describe the elastic behavior of concrete are the Poisson's ratio (υ) and the elastic modulus (E_c). As stipulated in ACI 318–19 [38], υ is considered to be 0.2 and $E_c = 4700\sqrt{f'_c}$, where f'_c is the unconfined compressive cylinder strength of concrete. The uniaxial compressive stress–strain relationship proposed by Saenz [57] was used to describe the nonlinear behavior of concrete, as follows:

Table 6
The CDPM parameters for concrete and SHCC adopted in the FEM.

	φ	ε	σ_{b0}/σ_{c0}	K	μ
Concrete	32°	0.10	1.16	0.667	0.0001
SHCC	30°	0.10	1.16	0.667	0.0001

φ = dilation angle; ε = Eccentricity ratio; σ_{b0}/σ_{c0} = the ratio of the biaxial/ uniaxial compressive strength; K = the shape coefficient; μ = viscosity parameter.

$$\sigma_c = \frac{E_c \varepsilon_c}{1 + (R + R_E - 2)\left(\frac{\varepsilon_c}{\varepsilon_0}\right) - (2R - 1)\left(\frac{\varepsilon_c}{\varepsilon_0}\right)^2 + R\left(\frac{\varepsilon_c}{\varepsilon_0}\right)^3} \quad (19)$$

where:

$$R = \frac{R_E(R_\sigma - 1)}{(R_\varepsilon - 1)^2} - \frac{1}{R_\varepsilon} \quad , R_E = \frac{E_c}{E_0} \quad , E_0 = \frac{f'_c}{\varepsilon_0} \quad (20)$$

where, σ_c, ε_c are the axial compressive strength and corresponding strain, ε_0 is the ultimate strain, E_0 is the secant modulus, $R_\varepsilon = 4$, $R_\sigma = 4$ as reported in [58].

However, for CFPSHT columns, the nonlinear behavior of confined concrete should be provided. That is because the SHCC tube could bear the vertical load and also confine the concrete core during the loading process. It has been widely stated in the literature that the behavior of confined concrete should be adopted when modeled using finite elements [59–62]. The compressive stress–strain curve of the confined concrete was taken as mentioned in the analytical study according to Popvics [46] and Mander [47].

Now, to get more accurate results for columns under eccentric compression, an eccentricity coefficient (ke,e) for the confinement stress should be taken into consideration. Hence, based on observation in this study, Eq. (21) can be derived as follows:

$$\frac{f'_{cc,e}}{f'_{cc,0}} = 1 - ke,e\left(\frac{e}{b}\right) \quad (21)$$

where, $f'_{cc,o}$ is the confined concrete stress under concentric loading, $f'_{cc,e}$ is the confined concrete stress corresponding to a given eccentricity ratio (e/b), and ke,e was found to be 0.61. when $e/b = 0$, $f'_{cc,e} = f'_{cc,o}$. It is worth noting that the given relation should not be treated as a general expression as it is expected to be influenced by the confinement ratio.

The Uniaxial behavior of concrete under tension is shown in Fig. 16 (a). The elastic parameters required to establish the first part of the relation are E_c and tensile strength, f_{ct}, where $f_{ct} = 0.33\sqrt{f'_c}$. The fracture energy method was used to specify the concrete post–peak tension failure behavior. The fracture energy can be estimated by $G_f = 110\left(\frac{f'_c}{10}\right)^{0.18}$ as proposed by Hillerborg [63], where G_f = fracture energy.

5.2.2. Strain–hardening cementitious composite (SHCC)

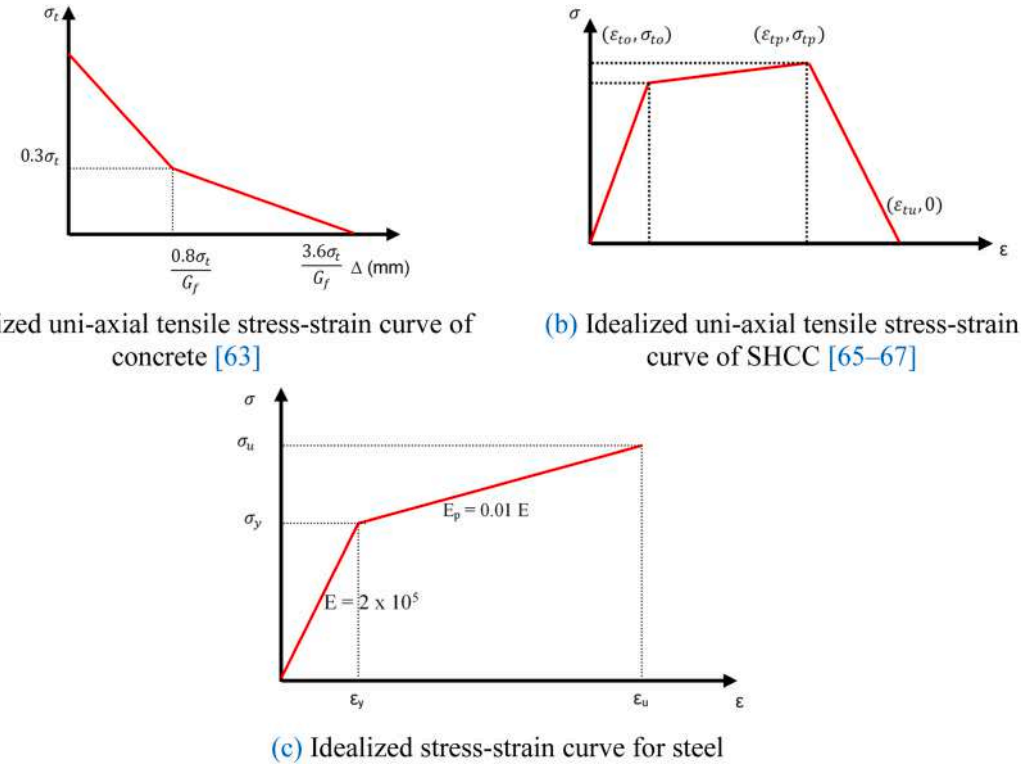
The compressive behavior of SHCC was modeled by entering the actual experimental stress–strain curve in the CDPM [64] and υ is considered to be 0.2. The plasticity parameters for SHCC were carefully calibrated with experimental results to get the best results as depicted in Table 6. Hence, the dilation angle (φ) was determined by sensitivity analysis and found to be 30°. The other plasticity parameters of the ratio of the biaxial/ uniaxial compressive strength, the flow potential eccentricity, and the shape coefficient adopted 1.16, 0.10, and 0.667, respectively. Meanwhile, the tensile behavior of SHCC was modeled by a tri–linear curve, Fig. 16 (b), as adopted by many researchers [65–67]. The experimental Uniaxial tensile stress–strain curve was therefore idealized into three distinct parts characterizing the tensile behavior: linear elastic behavior until ε_{to}, strain–hardening behavior associated with multiple cracking until ε_{tp}, and a softening behavior until ε_{tu}.

5.2.3. Reinforcing bars

The elastic behavior of steel material was defined by specifying Young's modulus (E_s) and Poisson's ratio (υ), of which typical values are 2×10^5 MPa and 0.30, respectively. The steel was assumed to be a bilinear elastic–plastic material with a stress–strain curve, as shown in Fig. 16 (c).

5.3. Validation of the FE modeling

Fig. 17 compares the columns experimentally observed failure modes with the FEM predicted failure modes (PE means plastic strains). It shows that the developed FEM could predict the mode of failure of the



(a) Idealized uni-axial tensile stress-strain curve of concrete [63]

(b) Idealized uni-axial tensile stress-strain curve of SHCC [65–67]

(c) Idealized stress-strain curve for steel

Fig. 16. Properties of used material in FEM simulation.

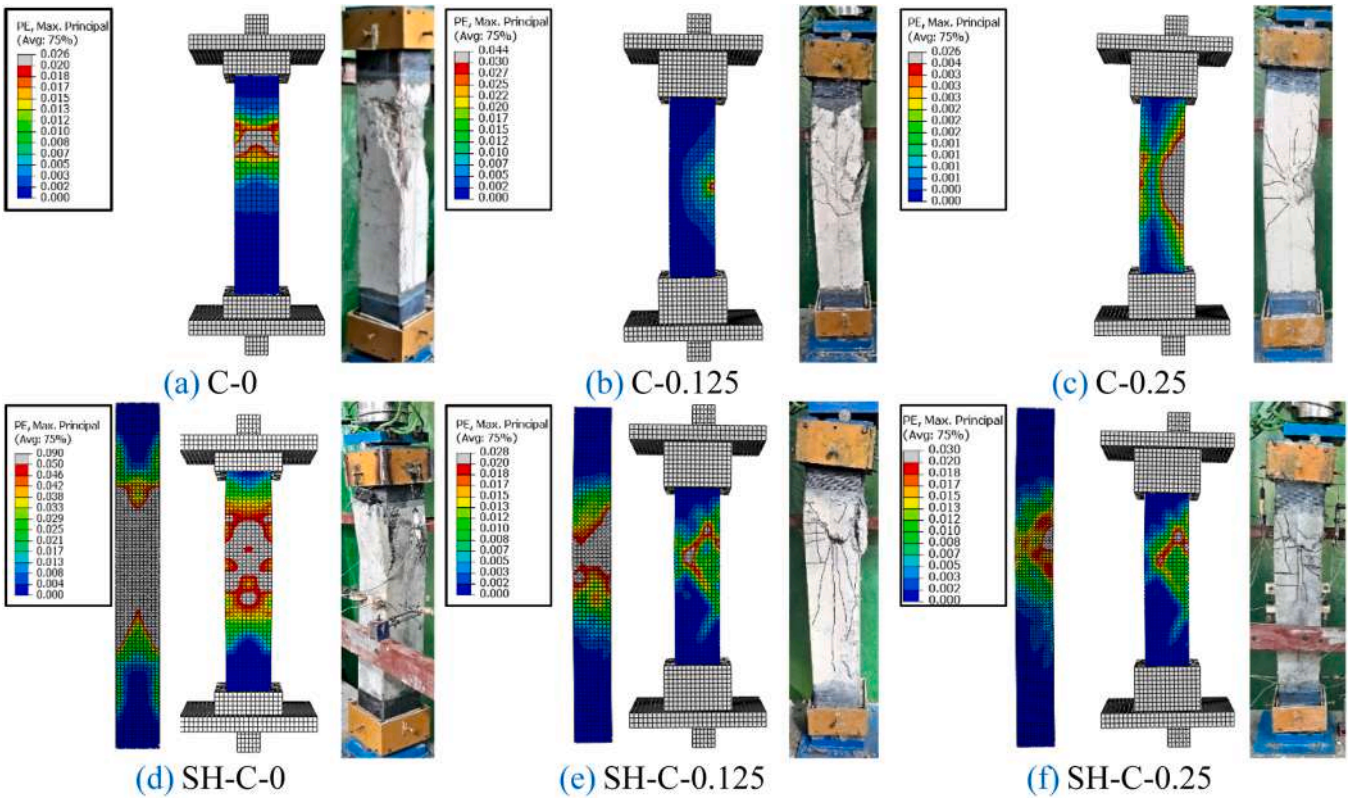


Fig. 17. Comparison between the mode of failure of experimental results and the FEM results for columns.

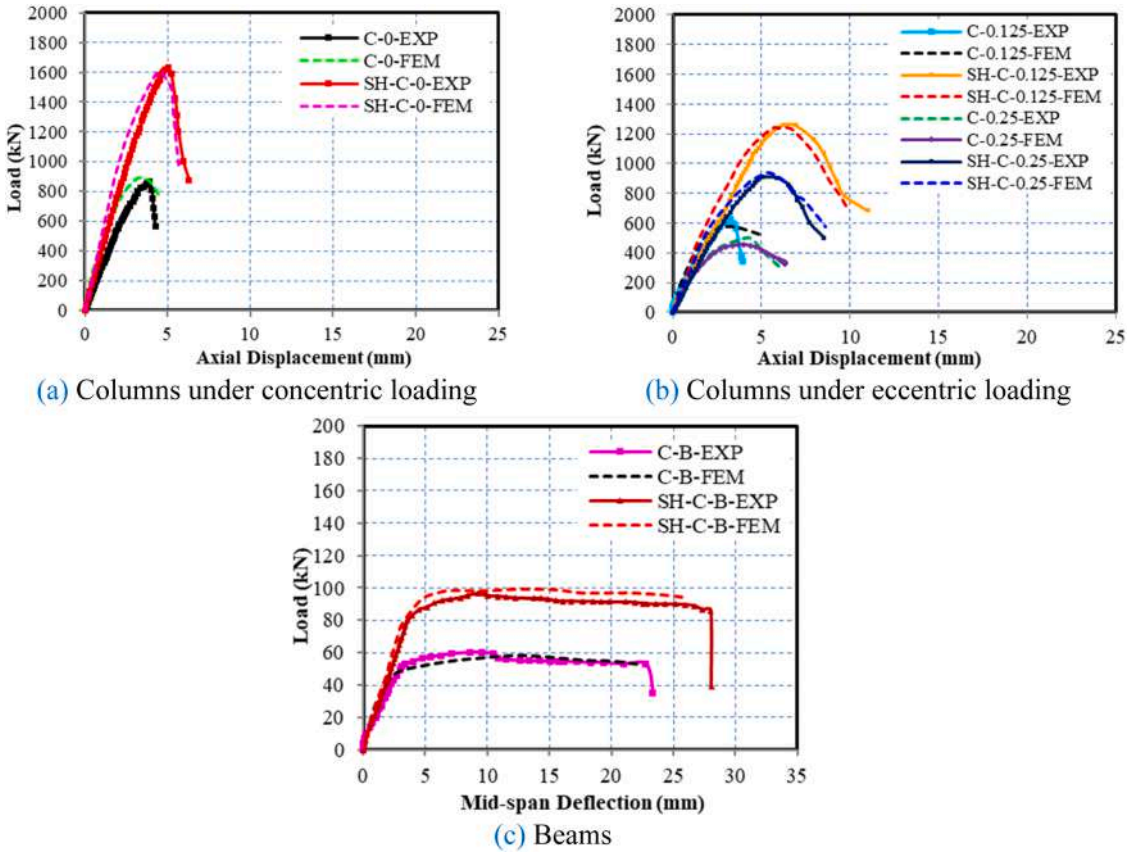


Fig. 18. Comparison of experimental, and FEM Load- Displacement curves for all specimens.

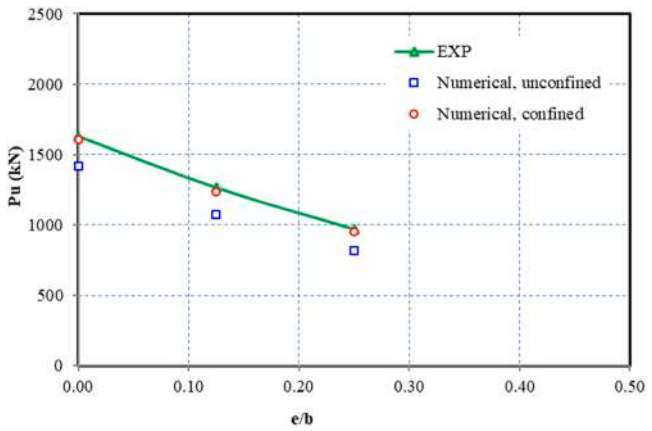


Fig. 19. Effect of confinement on FEM simulation.

proposed CFPSHT columns.

The FEM–predicted load–displacement curves are compared with the experimental curves in Fig. 18 for all specimens. These figures showed that the FEM load–displacement curves are in good agreement with those experimental curves. Also, as can be seen in Fig. 19, considering the effect of confinement in the FEM gives rise to a reasonable match between the experimental and FE results. The equation obtained in relation (21) provides an acceptable prediction of the confinement effect of the SHCC tube under eccentric loading.

6. Parametric study

According to the above analysis, FEM developed in this research could provide reasonably accurate predictions for the simulation of the compressive behavior of SHCC tubes filled with concrete based on the validations of the failure modes, and the load–displacement curves. Consequently, the effects of the SHCC tube thickness and the strength of the concrete core coupled with the eccentricity ratio on the performance of the CFPSHT column were discussed. Table 7 lists the description of the parameters studied in the parametric study.

6.1. Effect of the prefabricated SHCC tube thickness

The impact of the SHCC tube thickness on the composite column's load-moment (P–M) curves is depicted in Fig. 20. It is evident that increasing the thickness of SHCC tube leads to increase in column capacity with increasing eccentricity when the columns fail in compression failure (small eccentric loading), the effect of SHCC tube thickness in compression is higher than the effect when the column fails in tension. This can be attributed to the higher confinement and compressive strength of SHCC in compression.

6.2. Effect of concrete core strength

The impact of concrete core strength on the CFPSHT column P-M curves is shown in Fig. 21. When the column is loaded in a small eccentric compression state, it is discovered that the CFPSHT column load-carrying capacity improves with the concrete's compressive strength where the majority of the cross-section is under compression. On the other hand, when the column is loaded in a large eccentric compression state, the effect of concrete strength is negligible. The reason why is the fact that concrete has a significantly higher compressive strength than tensile strength.

7. Conclusions

This research presented an experimental investigation and FE simulation for the behavior of a column consisting of a prefabricated SHCC tube and conventional concrete. Four specimens were created by replacing part of the concrete with a prefabricated SHCC tube, while four specimens were made entirely of conventional concrete as the reference specimens. After executing the experiments, FE modeling was proposed to simulate and validate the tested specimens. This was done to allow a parametric study of numerous eccentricities, as well as a variety of concrete core strength and SHCC tube thicknesses. The key conclusions can be drawn as follows:

1. The failure mode of the CFPSHT columns differs significantly from the conventional concrete columns. All columns failed finally in compression; however, multiple cracks occurred on the surface of the

Table 7
The parameters in the parametric study.

Specimen	e (mm)	e/b	f'_c(MPa)	t_{SHCC}(mm)
SH–C	0	0.00	20	25
	25	0.125		
	50	0.25		
	75	0.375		
	100	0.50		
	125	0.625		
	150	0.75		
	175	0.875		
	B	B		
	0	0.00	20	35
	25	0.125		
	50	0.25		
	75	0.375		
	100	0.50		
	125	0.625		
	150	0.75		
	175	0.875		
	B	B		
	0	0.00	20	45
	25	0.125		
	50	0.25		
	75	0.375		
	100	0.50		
	125	0.625		
	150	0.75		
	175	0.875		
	B	B		
	0	0.00	28	35
	25	0.125		
	50	0.25		
	75	0.375		
	100	0.50		
	125	0.625		
	150	0.75		
	175	0.875		
	B	B		
	0	0.00	36	35
	25	0.125		
	50	0.25		
	75	0.375		
	100	0.50		
	125	0.625		
	150	0.75		
	175	0.875		
	B	B		
	0	0.00	44	35
	25	0.125		
	50	0.25		
	75	0.375		
	100	0.50		
	125	0.625		
	150	0.75		
	175	0.875		
	B	B		

f'_c= the unconfined compressive cylinder strength of concrete; t_{SHCC}= the thickness of the PSHCC tube.

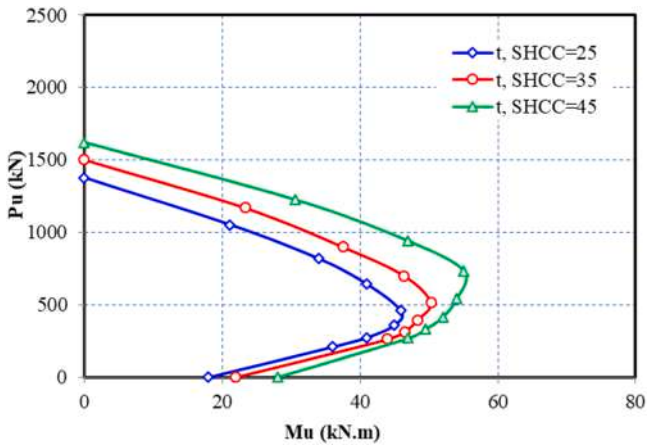


Fig. 20. Effect of the PSHCC tube thickness.

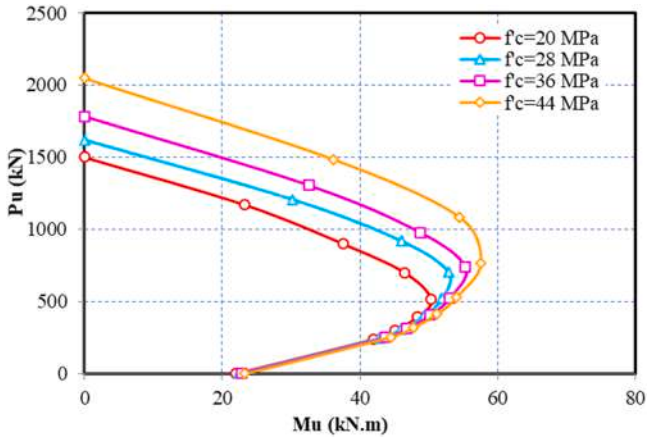


Fig. 21. Effect of concrete core strength.

SHCC tube, and no cover spalled until the end of the test, unlike conventional concrete columns, which exhibited severe cover spalling and concrete crushing.

2. The CFPSHT columns showed significant crack control ability compared to conventional columns under different load eccentricities. The maximum crack width was approximately 0.40 mm under 50 mm eccentricity.
3. The ultimate loads of the CFPSHT columns increased by approximately 88 % under concentric loading owing to SHCC's higher compressive and tensile strength as well as the confinement of the SHCC tube, while they increased by 101 % and 94 % in the case of eccentricity ratios of 0.125 and 0.25, respectively, compared to the conventional concrete column.
4. The analytical interaction diagram was in good agreement with the experimental results and the confinement effect of the SHCC tube on the concrete core should be taken into consideration.
5. Regarding the FE model, the proposed modeling of confined concrete under the confinement of the SHCC tube in case of eccentric loading could capture the mode of failure, ultimate loads, and the load–displacement behavior of the CFPSHT columns.
6. Increasing the thickness of the SHCC tube can effectively increase the ultimate load of the CFPSHT columns with both small and large eccentricities, but increasing the strength of concrete can only increase the ultimate load capacity of the CFPSHT columns with small eccentricities.

CRediT authorship contribution statement

Mohamed Hindawi: Writing – review & editing, Writing – original draft, Validation, Software, Methodology, Formal analysis, Data curation, Conceptualization. **Mohamed H. Mahmoud:** Writing – review & editing, Supervision, Methodology, Conceptualization. **Ahmed T. Baraghith:** Writing – review & editing, Writing – original draft, Supervision, Methodology, Formal analysis, Conceptualization. **Tarek F. El-Shafiey:** Writing – review & editing, Supervision, Methodology, Conceptualization.

Declaration of Competing Interest

The authors declare that they have no known competing financial interests or personal relationships that could have appeared to influence the work reported in this paper.

Data availability

The data are available only with direct contact through email to the corresponding author.

References

[1] Han LH, Hou CC, Wang QL. Behavior of circular CFST stub columns under sustained load and chloride corrosion. J Constr Steel Res 2014;103:23–36. https://doi.org/10.1016/j.jcsr.2014.07.021.
[2] Hou CC, Han LH, Wang QL, Hou C. Flexural behavior of circular concrete filled steel tubes (CFST) under sustained load and chloride corrosion. Thin-Walled Struct 2016;107:182–96. https://doi.org/10.1016/j.tws.2016.02.020.
[3] Ozbakkaloglu T, Saatcioglu M. Seismic performance of square high-strength concrete columns in FRP stay-in-place formwork. J Struct Eng 2007;133(1):44–56. https://doi.org/10.1061/(asce)0733-9445(2007)133:1(44).
[4] Wu YF, Wei Y. General stress-strain model for steel-and FRP-confined concrete. J Compos Constr 2015;19(4):04014069. https://doi.org/10.1061/(asce)cc.1943-5614.0000511.
[5] Hu YJ, Jiang C, Liu W, Yu QQ, Zhou YL. Degradation of the in-plane shear modulus of structural BFRP laminates due to high temperature. Sensors 2018;18(10):3361. https://doi.org/10.3390/s18103361.
[6] Hung CC, Chen YS. Innovative ECC jacketing for retrofitting shear-deficient RC members. Constr Build Mater 2016;111:408–18. https://doi.org/10.1016/j.conbuildmat.2016.02.077.
[7] Han LH, Hou CC, Wang QL. Behavior of circular CFST stub columns under sustained load and chloride corrosion. J Constr Steel Res 2014;103:23–36. https://doi.org/10.1016/j.jcsr.2014.07.021.
[8] Yang H, Han LH, Wang YC. Effects of heating and loading histories on post-fire cooling behaviour of concrete-filled steel tubular columns. J Constr Steel Res 2008;64(5):556–70. https://doi.org/10.1016/j.jcsr.2007.09.007.
[9] Irshidat MR, Al-Shannaq A. Using textile reinforced mortar modified with carbon nano tubes to improve flexural performance of RC beams. Compos Struct 2018;200:127–34. https://doi.org/10.1016/j.compstruct.2018.05.088.
[10] Chen X, Zhuge Y, Al-Gemeel AN, Xiong Z. Compressive behaviour of concrete column confined with basalt textile reinforced ECC. Eng Struct 2021;243:112651. https://doi.org/10.1016/j.engstruct.2021.112651.
[11] Shan B, Lai DD, Xiao Y, Luo XB. Experimental research on concrete-filled RPC tubes under axial compression load. Eng Struct 2018;155:358–70. https://doi.org/10.1016/j.engstruct.2017.11.012.
[12] Lai BL, Zhang MY, Chen ZP, Liew JR, Zheng YY. Axial compressive behavior and design of semi-precast steel reinforced concrete composite columns with permanent ECC formwork. In Structures, 57. Elsevier; 2023, November, 105130. https://doi.org/10.1016/j.istruc.2023.105130.
[13] Li VC, Stang H, Krenchel H. Micromechanics of crack bridging in fibre-reinforced concrete. Mater Struct 1993;26:486–94. https://doi.org/10.1007/bf02472808.
[14] Arain MF, Wang M, Chen J, Zhang H. Experimental and numerical study on tensile behavior of surface modified PVA fiber reinforced strain-hardening cementitious composites (PVA-SHCC. Constr Build Mater 2019;217:403–15. https://doi.org/10.1016/j.conbuildmat.2019.05.083.
[15] Li VC, Wang S, Wu C. Tensile strain-hardening behavior of polyvinyl alcohol engineered cementitious composite (PVA-ECC). Mater J 2001;98(6):483–92. https://doi.org/10.14359/10851.
[16] Yu K, Wang Y, Yu J, Xu S. A strain-hardening cementitious composites with the tensile capacity up to 8. Constr Build Mater 2017;137:410–9. https://doi.org/10.1016/j.conbuildmat.2017.01.060.
[17] Yang X, Gao WY, Dai JG, Lu ZD, Yu KQ. Flexural strengthening of RC beams with CFRP grid-reinforced ECC matrix. Compos Struct 2018;189:9–26. https://doi.org/10.1016/j.compstruct.2018.01.048.
[18] Swolfs Y, Meerten Y, Hine P, Ward I, Verpoest I, Gorbatikh L. Introducing ductility in hybrid carbon fibre/self-reinforced composites through control of the damage

mechanisms. Compos Struct 2015;131:259–65. https://doi.org/10.1016/j.compstruct.2015.04.069.
[19] Said SH, Razak HA. The effect of synthetic polyethylene fiber on the strain hardening behavior of engineered cementitious composite (ECC. Mater Des 2015;86:447–57. https://doi.org/10.1016/j.matdes.2015.07.125.
[20] Zhang J, Leung CK, Gao Y. Simulation of crack propagation of fiber reinforced cementitious composite under direct tension. Eng Fract Mech 2011;78(12):2439–54. https://doi.org/10.1016/j.engfracmech.2011.06.003.
[21] Hassan A, Baraghith AT, Atta AM, El-Shafiey TF. Retrofitting of shear-damaged RC T-beams using U-shaped SHCC jacket. Eng Struct 2021;245:112892. https://doi.org/10.1016/j.engstruct.2021.112892.
[22] Baraghith AT, Mansour W, Behiry RN, Fayed S. Effectiveness of SHCC strips reinforced with glass fiber textile mesh layers for shear strengthening of RC beams: experimental and numerical assessments. Constr Build Mater 2022;327:127036. https://doi.org/10.1016/j.conbuildmat.2022.127036.
[23] Deng M, Zhang Y, Li Q. Shear strengthening of RC short columns with ECC jacket: cyclic behavior tests. Eng Struct 2018;160:535–45. https://doi.org/10.1016/j.engstruct.2018.01.061.
[24] Leung CK, Cao Q. Development of pseudo-ductile permanent formwork for durable concrete structures. Mater Struct 2010;43:993–1007. https://doi.org/10.1617/s11527-009-9561-4.
[25] Qiao Z, Pan Z, Leung CKY, Meng S. Experimental study and analysis of flexural behavior of ECC/RC composite beams. J. Southeast Univ 2017;47:724–31. https://doi.org/10.1007/s11709-019-0556-0.
[26] Pan Z, Zhu Y, Qiao Z, Meng S. Seismic behavior of composite columns with steel reinforced ECC permanent formwork and infilled concrete. Eng Struct 2020;212:110541. https://doi.org/10.1016/j.engstruct.2020.110541.
[27] Kunieda M, Hussein M, Ueda N, Nakamura H. Enhancement of crack distribution of UHP-SHCC under axial tension using steel reinforcement. J Adv Concr Technol 2010;8(1):49–57. https://doi.org/10.3151/jact.8.49.
[28] Khalil AEHA, Atta AM, Baraghith AT, Behiry RN, Soliman OE. Shear strengthening of concrete deep beams using pre-fabricated strain-hardening cementitious composite plates. Eng Struct 2023;278:115548. https://doi.org/10.1016/j.engstruct.2022.115548.
[29] Afefy HMED, Mahmoud MH. Structural performance of RC slabs provided by pre-cast ECC strips in tension cover zone. Constr Build Mater 2014;65:103–13. https://doi.org/10.1016/j.conbuildmat.2014.04.096.
[30] Maalej M, Li VC. Introduction of strain-hardening engineered cementitious composites in design of reinforced concrete flexural members for improved durability. Struct J 1995;92(2):167–76. https://doi.org/10.14359/1150.
[31] Deng M, Zhang Y. Cyclic loading tests of RC columns strengthened with high ductile fiber reinforced concrete jacket. Constr Build Mater 2017;153:986–95. https://doi.org/10.1016/j.conbuildmat.2017.07.175.
[32] Hung CC, Chen YS. Innovative ECC jacketing for retrofitting shear-deficient RC members. Constr Build Mater 2016;111:408–18. https://doi.org/10.1016/j.conbuildmat.2016.02.077.
[33] Pan Z, Liu J, Wu C, Qiao Z, Leung C, Meng S. Experimental study and finite element analysis of seismic behavior of reinforced ECC. Compos Columns J Build Struct 2017;38:38–45.
[34] Wu C, Pan Z, Su RKL, Leung CK, Meng S. Seismic behavior of steel reinforced ECC columns under constant axial loading and reversed cyclic lateral loading. Mater Struct 2017;50:1–15. https://doi.org/10.1617/s11527-016-0947-9.
[35] Xu L, Pan J, Chen J. Mechanical behavior of ECC and ECC/RC composite columns under reversed cyclic loading. J Mater Civ Eng 2017;29(9):04017097. https://doi.org/10.1061/(asce)mt.1943-5533.0001950.
[36] Cai J, Pan J, Lu C. Mechanical behavior of ECC-encased CFST columns subjected to eccentric loading. Eng Struct 2018;162:22–8. https://doi.org/10.1016/j.engstruct.2018.02.029.
[37] Li F, Feng Z, Deng K, Yu Y, Hu Z, Jin H. Axial behavior of reinforced PP-ECC column and hybrid NSC-ECC column under compression. Eng Struct 2019;195:223–30. https://doi.org/10.1016/j.engstruct.2019.06.010.
[38] ACI Committee. Building code requirements for structural concrete (ACI 318-19) and commentary. Am Concr Inst Farming Hills, MI 2019:519.
[39] JSCE Recommendations for design and construction of high performance fiber reinforced cement composites with multiple fine cracks, 2008. Japanese Society of Civil Engineers, Tokyo, Japan.
[40] Yu KQ, Yu JT, Dai JG, Lu ZD, Shah SP. Development of ultra-high performance engineered cementitious composites using polyethylene (PE) fibers. Constr Build Mater 2018;158:217–27. https://doi.org/10.1016/j.conbuildmat.2017.10.040.
[41] Afefy HMED, Mahmoud MH. Structural performance of RC slabs provided by pre-cast ECC strips in tension cover zone. Constr Build Mater 2014;65:103–13. https://doi.org/10.1016/j.conbuildmat.2014.04.096.
[42] Shan B, Liu G, Li TY, Liu FC, Liu Z, Xiao Y. Experimental research on seismic behavior of concrete-filled reactive powder concrete tubular columns. Eng Struct 2021;233:111921. https://doi.org/10.1016/j.engstruct.2021.111921.
[43] Hadi MN, Goaiz HA, Yu T. Experimental investigation of CFRP confined hollow core Reactive Powder Concrete columns. Constr Build Mater 2018;174:343–55. https://doi.org/10.1016/j.conbuildmat.2018.04.087.
[44] Zhang Q, Xiao J, Zhang K, Duan Z. Mechanical behavior of seawater sea-sand recycled concrete columns confined by engineered cementitious composite under eccentric compression. J Build Eng 2022;45:103497. https://doi.org/10.1016/j.jobe.2021.103497.
[45] Ge W, Cai C, Ji X, Ashour AF, Cao D. Experimental study of mechanical properties of PVA-ECC under freeze-thaw cycles. J Test Eval 2018;46(6):2330–8. https://doi.org/10.1520/JTE20160145.
[46] Popovics S. A numerical approach to the complete stress-strain curve of concrete. Cem Concr Res 1973;3(5):583–99. https://doi.org/10.1016/0008-8846(73)90096-3.
[47] Mander JB, Priestley MJ, Park R. Theoretical stress-strain model for confined concrete. J Struct Eng 1988;114(8):1804–26. https://doi.org/10.1061/(asce)0733-9445(1988)114:8(1804).
[48] El-Shafiey, T.F., Hussein, M., Baraghith, A.T., Hindawi, M. Behaviour of Concrete Filled-Prefabricated UHP-SHCC Tubular Columns under Eccentric Loading. MSC Thesis; Tanta University; Egypt 2022.
[49] Teng JG, Huang YL, Lam L, Ye LP. Theoretical model for fiber-reinforced polymer-confined concrete. J Compos Constr 2007;11(2):201–10. https://doi.org/10.1061/(ASCE)1090-0268(2007)11:2(201).
[50] ABAQUS, 2022. ABAQUS Theory and User Manuals, version 6.22.
[51] Hemmati A, Kheyroddin A. Behavior of large-scale bracing system in tall buildings subjected to earthquake loads. J Civ Eng Manag 2013;19(2):206–16. https://doi.org/10.3846/13923730.2012.741613.
[52] Tian H, Zhou Z, Zhang Y, Wei Y. Axial behavior of reinforced concrete column with ultra-high performance concrete stay-in-place formwork. Eng Struct 2020;210:110403. https://doi.org/10.1016/j.engstruct.2020.110403.
[53] Fang C, Sadakkathulla MA, Sheikh A. Experimental and numerical study of ultra-high-performance fiber-reinforced concrete column subjected to axial and eccentric loads. Int J Civ Environ Eng 2019;13(2):79–85.
[54] Lubliner J, Oliver J, Oller S, Oñate E. A plastic-damage model for concrete. Int J Solids Struct 1989;25(3):299–326. https://doi.org/10.1016/0020-7683(89)90050-4.
[55] Lee J, Fenves GL. Plastic-damage model for cyclic loading of concrete structures. J Eng Mech 1998;124(8):892–900. https://doi.org/10.1061/(asce)0733-9399(1998)124:8(892).
[56] Barth KE, Wu H. Efficient nonlinear finite element modeling of slab on steel stringer bridges. Finite Elem Anal Des 2006;42(14-15):1304–13. https://doi.org/10.1016/j.finel.2006.06.004.
[57] Saenz LP. discussion of " Equation for the Stress-Strain Curve of Concrete" by Desayi and Krishnan. J Am Concr Inst 1964;61:1229–35. https://doi.org/10.14359/7785.
[58] Hu HT, Schnobrich WC. Constitutive modeling of concrete by using nonassociated plasticity. J Mater Civ Eng 1989;1(4):199–216. https://doi.org/10.1061/(asce)0899-1561(1989)1:4(199).
[59] Yu TTJG, Teng JG, Wong YL, Dong SL. Finite element modeling of confined concrete-I: drucker–prager type plasticity model. Eng Struct 2010;32(3):665–79. https://doi.org/10.1016/j.engstruct.2009.11.014.
[60] Karabinis AI, Rousakis TC, Manolitsi GE. 3D finite-element analysis of substandard RC columns strengthened by fiber-reinforced polymer sheets. J Compos Constr 2008;12(5):531–40. https://doi.org/10.1061/(asce)1090-0268(2008)12:5(531).
[61] Yu T, Teng JG, Wong YL, Dong SL. Finite element modeling of confined concrete-II: plastic-damage model. Eng Struct 2010;32(3):680–91. https://doi.org/10.1016/j.engstruct.2009.11.013.
[62] Tao Z, Wang ZB, Yu Q. Finite element modelling of concrete-filled steel stub columns under axial compression. J Constr Steel Res 2013;89:121–31. https://doi.org/10.1016/j.jcsr.2013.07.001.
[63] Hillerborg A. The theoretical basis of a method to determine the fracture energy GF of concrete. Mater Struct 1985;18:291–6. https://doi.org/10.1007/bf02472919.
[64] Hemmati A, Kheyroddin A, Sharbatdar MK. Plastic hinge rotation capacity of reinforced HPFRCC beams. J Struct Eng 2015;141(2):04014111. https://doi.org/10.1061/(asce)st.1943-541x.0000858.
[65] Meng D, Huang T, Zhang YX, Lee CK. Mechanical behaviour of a polyvinyl alcohol fibre reinforced engineered cementitious composite (PVA-ECC) using local ingredients. Constr Build Mater 2017;141:259–70. https://doi.org/10.1016/j.conbuildmat.2017.02.158.
[66] Kabir MI, Lee CK, Rana MM, Zhang YX. Flexural and bond-slip behaviours of engineered cementitious composites encased steel composite beams. J Constr Steel Res 2019;157:229–44. https://doi.org/10.1016/j.jcsr.2019.02.032.
[67] Rana MM, Lee CK, Al-Deen S, Zhang YX. Flexural behaviour of steel composite beams encased by engineered cementitious composites. J Constr Steel Res 2018;143:279–90. https://doi.org/10.1016/j.jcsr.2018.01.004.